Mon. Not. R. Astron. Soc. **000**, 000–000 (0000) Printed 4 November 2015 (MN LATEX style file v2.2)

The X-ray dust scattered rings of the black hole low mass binary V404 Cyg

G. Vasilopoulos[1⋆] & M. Petropoulou[2†]
[1]*Max-Planck-Institut für extraterrestrische Physik,Giessenbachstraße, 85748 Garching, Germany*
[2] *Department of Physics and Astronomy, Purdue University, 525 Northwestern Avenue, West Lafayette, IN 47907, USA*

arXiv:1511.00932v1 [astro-ph.HE] 3 Nov 2015

Received ?? ??? 2015 / Accepted ?? ??? 2015

ABSTRACT

We report on the first detection of X-ray dust scattered rings from the Galactic low mass X-ray binary V404 Cyg. The observation of the system with *Swift*/XRT on June 30 2015 revealed the presence of five concentric ring-like structures centred at the position of V404 Cyg. Follow-up *Swift*/XRT observations allowed a time-dependent study of the X-ray rings. Assuming that these are the result of small-angle, single X-ray scattering by dust grains along the line of sight, we find that their angular size scales as $\theta \propto \sqrt{t}$ in agreement with theoretical predictions. The dust grains are concentrated in five dust layers located at about 2.12, 2.05, 1.63, 1.50 and 1.18 kpc from the observer. These coincide roughly with locations of enhanced extinction as determined by infrared photometry. Assuming that the grain size distribution is described by a generalized Mathis-Rumpl-Nordsieck model, we find that the power-law index of the most distant cloud is $q \sim 4.4$, while $q \sim 3.5 - 3.7$ in all other clouds. We constrain at a 3σ level the maximum grain size of the intermediate dust layers in the range $0.16 - 0.20\,\mu$m and set a lower limit of $\sim 0.2\,\mu$m in the other clouds. Hints of an exponential cutoff at the angular intensity profile of the outermost X-ray ring suggest that the smallest grains have sizes $0.01\mu\text{m} \leqslant \alpha_{\rm min} \lesssim 0.03\,\mu$m. Based on the relative ratios of dust column densities we find the highest dust concentration at ~ 1.6 kpc. Our results indicate a gradient in the dust properties within 1 kpc from V404 Cyg.

Key words: X-ray: binaries – individual: V404 Cygni – X-ray: ISM – (ISM:) dust

1 INTRODUCTION

V404 Cyg, also known as GS 2023+338, is a nearby (d = 2.39 ± 0.14 kpc Miller-Jones et al. 2009) low mass X-ray binary (LMXB) with an orbital period of ∼ 6.47 d (see e.g. Casares et al. 1992; Casares & Charles 1994). It consists of a ∼ 1 $M_\odot$ late type G or early type K companion star (Casares et al. 1992; Wagner et al. 1992; Casares & Charles 1994) and a compact object. The latter is black hole (BH) with an estimated mass of $12^{+3}_{-2} M_\odot$ (Shahbaz et al. 1996) (for other BH mass estimates, see Casares et al. 1992; Casares & Charles 1994). V404 Cyg is an X-ray transient source with three confirmed historical outbursts in 1936, 1958 and 1989 (Richter 1989). It was in the 1989 outburst (for a detailed analysis, see Życki et al. 1999) that V404 Cyg was discovered in X-rays by the Geminga satellite (Makino et al. 1989).

After a long period of quiescence (26 yr), the Swift Burst Alert Telescope (BAT) was triggered on June 15 2015 (18:32 UT) following the systems re-brightening (Barthelmy et al. GCN #17929). Soon after the BAT trigger, the system was detected in X-rays by MAXI on board of the International Space Station (Negoro et al. 2015), which initiated multi-wavelength observations of the source (see e.g. Garner et al. 2015; Gazeas et al. 2015; Mooley et al. 2015; Tetarenko et al. 2015). The subsequent, still ongoing, monitoring of the renewed activity of V404 Cyg across the electromagnetic spectrum resulted in observations that can be used not only for studying the properties of the LMXB itself (e.g. King et al. 2015; Rodriguez et al. 2015a) but also those of its surrounding medium. For the latter, the detection, for the first time, of ring-like structures centered at the position of V404 Cyg having a typical angular size of a few arcmin (Beardmore et al. 2015), is of particular importance. The formation of the X-ray rings can be understood in terms of scattering of the source's X-ray photons by dust grains of the interstellar medium (ISM), and in this regard, their study can provide information for the properties of the ISM and the dust distribution in the direction of the source.

It was originally proposed by Overbeck (1965) that a bright X-ray point source would appear surrounded by a diffuse X-ray emission (halo) due to the small angle scattering from dust grains in the ISM. First observational evidence for the X-ray scattering from interstellar grains were presented by Rolf (1983) for the source GX3394. As the scattering cross section depends on the properties of the dust grains, such as size and composition, as well as on the distribution of dust along the line of

⋆ Email: gevas@mpe.mpg.de
† Einstein Postdoctoral Fellow

© 0000 RAS

sight (LOS) (van de Hulst 1957), analysis of X-ray halos from Galactic and extragalactic sources can be used for determining the properties of the interstellar dust (e.g. Mauche & Gorenstein 1986; Greiner et al. 1995; Predehl & Schmitt 1995; Greiner et al. 1996; Predehl & Klose 1996; Draine & Tan 2003; Costantini et al. 2005; Smith et al. 2006; Corrales & Paerels 2015). If the spatial distribution of dust in the direction of a variable X-ray source is known, constraints to the source distance can be then set by using the time delay between the direct and scattered signals (Trümper & Schönfelder 1973). This method has been applied to several systems, including the X-ray binaries Cyg X-3 (Predehl et al. 2000) and Cyg X-1 (Xiang et al. 2011), as well as and the soft gamma-ray repeater (SGR) SGR 1806-20 (Svirski et al. 2011).

Although the scattering from bright X-ray point sources manifests itself usually as an X-ray halo (e.g. Rolf 1983), the combination of a short duration outburst from a variable X-ray source with a series of discrete dust slabs along the LOS would result in the appearance of multiple (typically, one or two) X-ray rings. Analysis of dust scattered rings have been applied to a variety of systems, such as gamma-ray bursts (GRBs) (e.g. Klose 1994; Vaughan et al. 2004; Vianello et al. 2007, and references therein), anomalous X-ray pulsars (see Tiengo et al. 2010, for 1E1547.05408), and SGR (e.g. Kouveliotou et al. 2001).

Here we report on the recent *Swift*/XRT observations of the first ever observed dust scattered X-ray rings from V404 Cyg. These observations offer a unique opportunity to study the properties of dust along the LOS in the direction of V404 Cyg for a number of reasons: (i) at least five dust scattered X-ray rings can be identified in the X-ray image, while in most cases the maximum number of observed rings is two to three; (ii) the expansion of the five rings can be followed for a minimum period of ~23 d for the outer ring, up to a maximum period of ~36 d for the innermost rings; (iii) V404 Cyg is one of the nearest, most luminous LMXB in quiescence (Miller-Jones et al. 2009); and (iv) its distance is well constrained. Aim of our study is to derive the basic properties of the dust, such as their spatial distribution and typical size, by applying a simple, yet well proven theoretical framework, to the recent *Swift*/XRT observations.

The present paper is structured as follows. In §2 we outline the basic formalism used in our analysis of the X-ray dust scattering. We report on the observations and the data reduction in §3. We continue in §4 with a presentation of our analysis and results. In §5 we discuss several aspects of our analysis and conclude in §6 with a summary of our results.

2 THEORETICAL FRAMEWORK

The dust grains in the ISM are responsible for X-ray scattering and absorption. The latter becomes important especially at energies below 1 keV, although the dust grains may be composed by elements with K-shell edges above 1 keV (see e.g. Smith & Dwek 1998). Moreover, the analytic Rayleigh-Gans (RG) approximation for the scattering cross section $d\sigma/d\Omega$ breaks down at energies $E < 1$ keV, where one should use the solution of Mie theory (van de Hulst 1957). We note that a detailed treatment of the X-ray scattering goes even beyond the Mie solution, as this is also derived under certain simplifying assumptions, e.g. spherical shape, that may not be satisfied for the dust grains of the ISM.

Here, we limit our analysis at $E \geqslant 1$ keV where X-ray absorption is not as important as in lower energies and make use of the RG approximation, which roughly speaking, is valid for photon energies in keV significantly larger than the grain size in μm. Furthermore, we neglect the effects of multiple X-ray scatterings, which become important if the scattered intensity is comparable to the intensity of the point source. This translates to $\tau_{\rm sc} > 1.3$ at 1 keV (Mathis & Lee 1991), where $\tau_{\rm sc}$ is the optical depth for scattering by dust. We can estimate $\tau_{\rm sc}$ for V404 Cyg using the relation $\tau_{\rm sc} \approx 0.15\, A_{\rm V} (1\,{\rm keV}/E)^{-1.8}$ (Draine & Bond 2004), where $A_{\rm V}$ is the visual extinction in the direction of the source. By adopting $A_{\rm V} \sim 4$ (Casares et al. 1993), we find $\tau_{\rm sc} \sim 0.6$ at 1 keV; this value would be lower by a factor of ~ 2, if the relation of Predehl & Schmitt (1995) was used. It is, therefore, reasonable to assume that multiple X-ray scatterings are not important for our study. Our results should be considered in the light of these assumptions.

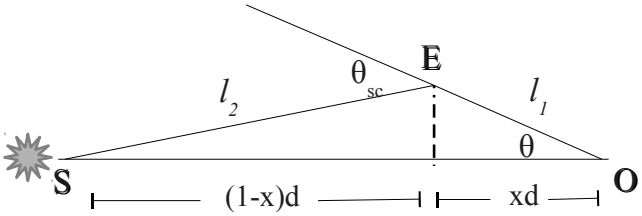

Figure 1. Sketch of the dust scattering geometry.

The observed time delay Δt between the X-ray outburst from the source and the detection of the X-ray dust scattered rings is the result of different path lengths (see e.g. Fig. 1), and is given by

$$\Delta t = \frac{\ell_1 + \ell_2}{c} - \frac{d}{c}, \tag{1}$$

where $\ell_1 = xd/\cos\theta$, $\ell_2 = \sqrt{(1-x)^2 d^2 + (xd)^2 \tan\theta^2}$, θ is the observed angular radius of the ring and xd is the distance of the dust screen from the observer. Expression (1) is derived under the assumption that the dust scattered rings observed at time t are the result of a single, short duration outburst occurring at t_0; this is reasonable as long as $\delta t \ll \Delta t$, where δt is the outburst duration. In the limit of small angles ($\theta \ll 1$), where $\tan\theta \approx \theta + O(\theta^3)$ and $\cos\theta \approx 1 - \theta^2/2$, the time delay for each ring is approximately given by

$$\Delta t \approx \frac{d}{2c}\frac{x}{1-x}\theta^2 + O(\theta^3). \tag{2}$$

The above expression may be rewritten in a more useful form as

$$\theta(t) = 1\ {\rm arcmin} \left(\frac{19.84(1-x)}{x}\right)^{1/2} \left(\frac{1\ {\rm kpc}}{d}\right)^{1/2} \left(\frac{\Delta t}{1\ {\rm d}}\right)^{1/2}. \tag{3}$$

In the RG approximation of small scattering angles ($\theta_{\rm sc}$) the cross section is written as (e.g Mauche & Gorenstein 1986):

$$\frac{d\sigma(E,\bar{\alpha},\theta_{\rm sc})}{d\Omega} = C_{\rm d}(E)\, \bar{\alpha}^6 e^{-\theta_{\rm sc}^2/2\Theta^2(E,\bar{\alpha})}, \tag{4}$$

where

$$\Theta(E,\bar{\alpha}) = \frac{1.04\ {\rm arcmin}}{E_{\rm keV}\bar{\alpha}}, \tag{5}$$

with $E_{\rm keV} \equiv E/1$ keV and $\bar{\alpha} \equiv \alpha/1\ \mu$m. The normalization of the scattering cross section is given by (Mauche & Gorenstein 1986)

$$C_{\rm d}(E) = 1.1 \left(\frac{2Z}{M}\right)^2 \left(\frac{\rho}{3\ {\rm gr\ cm^{-3}}}\right)^2 \left(\frac{F(E)}{Z}\right)^2\ {\rm cm^2\ sr^{-1}}. \tag{6}$$

In the above, Z is the atomic number, M is the molecular mass (in amu), ρ is the mass density, E is the X-ray energy in keV and $F(E)$

is the form factor (Henke 1981). The factor $F(E)/Z$ is close to unity when considering the scattering of X-rays with energies 1-6 keV, since most of the K-edges of light elements ($Z \leqslant 10$) lie below this range[1] (Dewey et al. 1969). Moreover, the factor $2Z/M$ is of order unity for all the abundant elements in grains (see e.g. Mathis & Lee 1991), and 3 gr cm^{-3} is the typical mass density of dust grains (see e.g. Mathis et al. 1977; Draine 2011).

For the general case of a continuous dust distribution between the source and the observer, the scattered intensity (in units of erg cm^{-2} s^{-1} keV^{-1} sr^{-1}) is given by (e.g. Mathis & Lee 1991):

$$I_{\rm sc}(\theta,E) = F_{\rm X}(E) N_{\rm H} \int_{\alpha_{\rm min}}^{\alpha_{\rm max}} d\alpha\, n(\alpha) \int_0^{1-\epsilon} dx\, \frac{f(x)}{(1-x)^2} \frac{d\sigma(E,\alpha,\theta_{\rm sc})}{d\Omega} \quad (7)$$

where θ is the observed angle, $F_{\rm X}(E)$ is the observed (i.e., not corrected for absorption) differential energy flux of the source (in erg cm^{-2} s^{-1} keV^{-1}), $N_{\rm H}$ is the total hydrogen column density along the LOS, $n(\alpha)$ is the number of grains per hydrogen atom with radii between α and $\alpha + d\alpha$, $f(x)$ is the spatial distribution of grains, normalized to unity for the interval (0,1) and $\epsilon \approx \theta$ for small θ, i.e. up to several arcmin (Smith & Dwek 1998). In the case where a spatially discrete distribution of dust is implied by the observations (i.e. rings vs. diffuse halo), we may write $f(x) = \sum_{i=1}^{N} \delta(x - x_i)$ (see also Mauche & Gorenstein 1986) and eq. (7) becomes $I_{\rm sc}(\theta,E) = \sum_{i=1}^{N} I_{\rm sc,i}(\theta,E)$, where

$$I_{\rm sc,i}(\theta,E) = F_{\rm X}(E) N_{\rm H,i} \frac{1}{(1-x_{\rm i})^2} \int_{\alpha_{\rm min,i}}^{\alpha_{\rm max,i}} d\alpha\, n_{\rm i}(\alpha) \frac{d\sigma(E,\alpha,\theta_{\rm sc})}{d\Omega}, \quad (8)$$

where $N_{\rm H,i}$ is the hydrogen column density of the cloud. For an X-ray burst of fluence $\Phi_{\rm X}(E)$ (in erg cm^{-2} keV^{-1}) that leads to the production of ring-like structures instead of an X-ray halo, eq. (8) becomes

$$F_{\rm sc,i}(\theta,E) = \Phi_{\rm X}(E) N_{\rm H,i} \frac{g(x)}{(1-x_{\rm i})^2} \int_{\alpha_{\rm min,i}}^{\alpha_{\rm max,i}} d\alpha\, n_{\rm i}(\alpha) \frac{d\sigma(E,\alpha,\theta_{\rm sc})}{d\Omega}, \quad (9)$$

where $g(x) \equiv 2\pi\theta d\theta/dt = 2\pi c(1-x)/xd$ (see eq. (2)) and $F_{\rm sc,i}$ is the scattered flux integrated over the angular extend of the X-ray ring (in erg cm^{-2} s^{-1} keV^{-1}).

For a power-law size distribution, i.e. $n(\alpha) \propto \alpha^{-q}$, the radial profile of the scattered intensity (or flux) from one dust layer should exhibit two power-law segments ($I_{\rm sc} \propto$ const for $\theta \lesssim \theta_1$, where θ_1 is given by eq. (5) for $\alpha = \alpha_{\rm max}$, and $I_{\rm sc} \propto \theta^{-7+q}$) followed by an exponential cutoff at an angle determined by the smallest size grains (see e.g. Svirski et al. 2011).

Although a power-law distribution is scale-free, in the case of X-ray scattering by a power-law grain distribution, an average grain size can still be defined (Mauche & Gorenstein 1986), since the scattering cross section introduces a characteristic grain size (see e.g. eqs. (4) and (5)). Using the integrated cross section over scattering angles, i.e.

$$\sigma(E,\bar{\alpha}) = 6.3\times10^{-7}\, \bar{\alpha}^4 \left(\frac{2Z}{M}\right)^2 \left(\frac{\rho}{3\ {\rm gr\ cm^{-3}}}\right)^2 \left(\frac{F(E)}{Z}\right)^2 {\rm cm}^2 \quad (10)$$

the average grain size is calculated by

$$\langle\alpha\rangle = \frac{\int d\alpha\, \sigma(E,\alpha)\alpha n(\alpha)}{\int d\alpha \sigma(E,\alpha) n(\alpha)} \approx \frac{5-q}{6-q}\alpha_{\rm max}, \quad (11)$$

where the approximation holds for $q < 5$. Equation (11) will be used to derive the average dust grain size using the best-fit results for q and $\alpha_{\rm max}$ (see §4).

3 OBSERVATIONS AND DATA REDUCTION

For the study of the X-ray rings we used *Swift*/XRT data which are publicly available from the `Swift Data Center`[2]. We ran the standard XRT pipeline to derive the cleaned event lists from the level one products. The observations were performed in two instrument modes, photon counting (PC) and window timing (WT) mode. For the WT data we kept single and double pixel events (grades 0-2), while for the PC data analysis we used single to quadruple events (grades 0-12).

The *Swift*/XRT data reduction and the analysis of the radial profiles of the X-ray rings was performed with the use of standardized procedures from the `ftools`[3] software packages. For the creation of the *Swift*/XRT light curve we used the `HEASoft` program `xselect`. The source events were extracted from a 40″region, while a similar size region was used for the background. The background correction was made by using the standard `FTool lcmath`.

The position of V404 Cyg on each of the images was calculated using the `xrtcentroid` tool, and the derived value was adopted as the center for all the X-ray rings displayed on the image under study. Finally, the radial profiles of the rings count rate per unit area were extracted by using the `ximage` program.

For the event selection/extraction of the individual rings we used the `HEASoft` program `xselect`. The X-ray spectra of the rings ware extracted from an annulus with inner and outer radii determined from the best fit radial profile of the ring (details about the fitting procedure can be found at §4). The `xrtmkarf` task was used to create the ancillary response function (ARF) used for the spectral analysis. The ARF was created for an extended source without PSF corrections from the vignetting-corrected exposure map.

For those *Swift*/XRT snapshots where the rings were partially outside the field-of-view (FOV) of the telescope, appropriate correction factors were estimated taking into account the extraction region and the exposure map of the instrument. The corrections were finally used as a scaling factor for the intensities derived after the fitting of the X-ray spectra.

Throughout the monitoring of the system (MJD 57203.5-57239.5) the X-ray rings could always be easily distinguished. To be exact, this holds for the two innermost rings, while the two intermediate rings were clearly visible until MJD 57231.3 and the outermost ring could not be detected after MJD 57226.5. For the four inner rings we chose to perform the analysis in pairs. This approach was adopted since their positions were separated by less than the full width at half maximum (FWHM) of their radial profiles, thus their properties could not be disentangled. Additionally by summing the detected photons of two adjacent rings we improved the signal-to-noise of our data. In order to test that this merging did not affect the results of our analysis, we extracted partially the X-ray spectrum from different regions of the double peaked radial profile and repeated the same analysis; in both cases, we found similar results.

The extracted X-ray spectra were then analyzed with `xspec` (Arnaud 1996) version 12.8.0. All the spectra were fitted with a phenomenological model of an absorbed power-law

[1] A table for X-ray absorption edges and lines can be found at http://www.kayelaby.npl.co.uk/atomic_and_nuclear_physics/4_2/4_2_1.html

[2] http://swift.gsfc.nasa.gov/sdc/

[3] https://heasarc.gsfc.nasa.gov/ftools/

(`tbnew*powerlaw`) and the elemental abundances of the ISM were set after Wilms et al. (2000). Due to the lack of photons of energies higher than 4 keV, the spectra were fitted in the energy range of 0.7-4 keV. The regions for determining the background contamination of the spectra were selected from annuli at the edges of the rings in study. The size of each annulus was based on the radial profile of the dust scattered rings. Details about the background selection can be found in §4.3. By fitting first all the X-ray spectra with χ^2-statistics, we obtained reduced χ^2 values between 0.8 and 1.4 that justify the absorbed power-law model selection. For those observations with sufficient statistics ($\gtrsim$ 400 counts) the binned spectra were then used and fitted with χ^2-statistics. In all other cases, the un-binned spectra were used and fitted with C-statistics (Cash 1979). From the best-fit model we then derived the intensity values at 1.0, 1.5, 2.0 and 2.5 keV. The observation log of the 23 *Swift*/XRT observations used for the analysis of the dust scattered rings can be found in Table A1 of appendix A where they are listed in ascending order with respect to their starting time of observation.

For the study of the overall activity of the system we additionally used all available INTEGRAL data. The satellite started monitoring the source from revolution 1554 till revolution 1563 with data made immediately public. Observations made during Revolutions 1555 and 1556 were done under an AO-12 approved Target-of-Opportunity program (PI: Rodriguez). The PI has kindly allowed public access to the data in the consolidated version[4] (Rodriguez et al. 2015a; Kuulkers 2015).

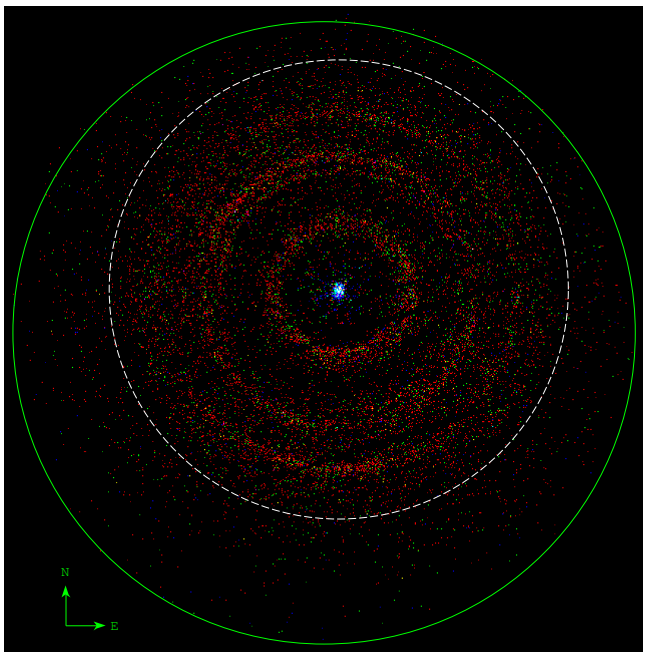

Figure 2. RGB image of the X-ray dust scattered rings observed by *Swift*/XRT at MJD 57205.5 (*Swift* OBS-ID 00033861006). The color coding used is R: 0.5-1.5 keV, G: 1.5-2.5 keV, and B: 2.5-10 keV. The *Swift*/XRT field-of-view is enclosed by the green circle, while a white circle of radius 9′ is overplotted for guiding the eye.

4 ANALYSIS AND RESULTS

4.1 Ring expansion

The radial expansion of the dust rings was modeled using the 1-10 keV *Swift*/XRT data, noting, however, that the dust scattered emission falls off rapidly at energies $\gtrsim$ 2.5 keV. This is also illustrated in Fig. 2 where only the central source is detected in the energy band 2.5-10 keV. Although we limited the analysis of XRT data above 1 keV, where approximate expressions for the scattering cross section from dust are applicable (for more details, see §2), we verified that our results on the location and expansion of the rings are not affected by the inclusion of lower energy X-ray data.

To model the angular profile of the dust scattered X-ray emission and to pinpoint the angular sizes of the rings, we assumed a uniform background that was optimized and then subtracted from the data. As we discuss in more detail in §4.3, the evolution of the angular profiles with time reveals a a variable background emission, which is, most probably, related to the V404 Cyg activity since its trigger. The background subtracted angular profiles of the dust scattered emission exhibit five major peaks that are related to the five ring-like structures observed with *Swift*/XRT. From this point on, we will refer to them as follows: the two innermost rings or "rings 1 and 2"; the two intermediate rings or "rings 3 and 4"; and the outermost ring or "ring 5".

We fitted the background subtracted angular profile using a model that consists of a King profile and five Lorentzian functions (f_L) with three free parameters each:

$$f_L^{(i)} = \frac{1}{4\pi} \frac{f_{0i}\gamma_i}{\sqrt{(r - r_{0i})^2 + \left(\frac{\gamma_i}{2}\right)^2}},\ i = 1, \ldots, 5. \tag{12}$$

In the above expression, $f_L^{(i)}$ is in units of ct s^{-1} arcmin^{-2} and r_{0i}, γ_i are in arcsec. The use of Lorentzian functions over-imposed on a King profile for modeling the observed radial profile of the dust rings is motivated by the following:

(i) the point spread function (PSF) of *Swift*/XRT is well modeled by a King profile (Moretti et al. 2005).

(ii) simulations performed by Tiengo et al. (2010) for the radial profile of a thin ring that is broadened by a PSF with King profile showed that a Lorentzian gives a better description than a Gaussian function. We verified that the replacement of the Lorentzian with Gaussian functions leads to poor fits, except for observations with poor signal to noise ratio between the ring profile and the local background or in cases where the X-ray ring is projected near the edge of the FOV of *Swift*/XRT, such as observation #19 (MJD 57223.4). In this case, the outermost ring was better described by a Gaussian function.

In short, in all cases but one we applied the two-component model described above. The observed radial profiles (symbols) and the best-fit models (solid lines) for an indicative subset of the analyzed observations are shown in Fig. 3, while the rest are presented in Fig. B1 of Appendix B. The position of the peaks and their errors, which are used in our subsequent analysis, are summarized in Table B1. Inspection of Fig. 3 shows that the best-fit model is particularly successful in capturing the peaks of the angular profile, and in most cases, it provides a good description of the data. However, for some observations, e.g. #1 and #2, the reduced χ^2 value of the global fit is high. This suggests that the two-component model

[4] These are available in the following link: http://www.isdc.unige.ch/integral/Operations/Shift/QLAsources/V404_Cygni/V404_Cygni.php

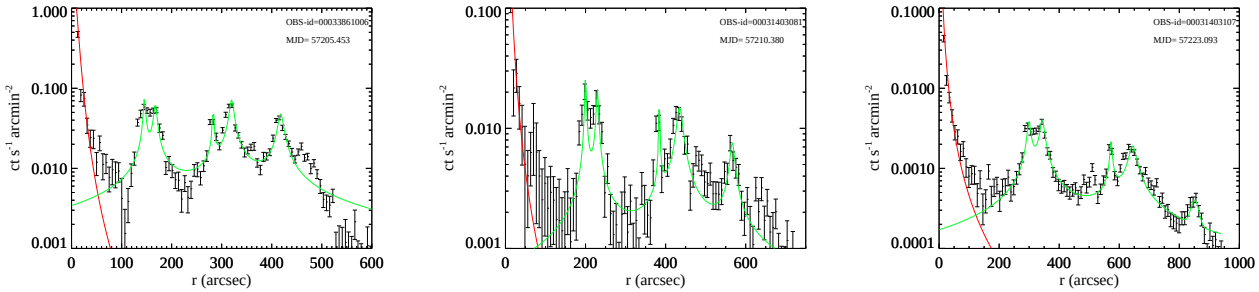

Figure 3. The background subtracted radial profile of the dust rings for three indicative *Swift*/XRT observations obtained in PC mode. The fitted model is composed by a King profile (red line) and five Lorentzian functions (green line). In some observations, such as # 19, the outermost ring (ring 5) was best modeled by a Gaussian function.

Table 1. Fitting parameters for the ring expansion using eq. (3).

Ring #	t_0 [MJD-57190]	x_i [a]	d_i [kpc]
1	9.81±0.12	0.8866±0.0006	2.12±0.12(0.002)[b]
2	9.71±0.10	0.8576±0.0006	2.05±0.12(0.001)
3	9.62±0.06	0.6839±0.0007	1.63±0.10(0.001)
4	9.64±0.03	0.6300±0.0003	1.50±0.09(0.001)
5	9.73±0.05	0.4958±0.0006	1.18±0.07(0.001)

[a] The values are calculated by fixing t_0 = 57199.75 d and performing a fit with only one free parameter.
[b] The error listed outside the parenthesis is the total one, i.e. calculated using error propagation, whereas the one enclosed in the parenthesis is the 1σ statistical error derived from the fit of the ring expansion.

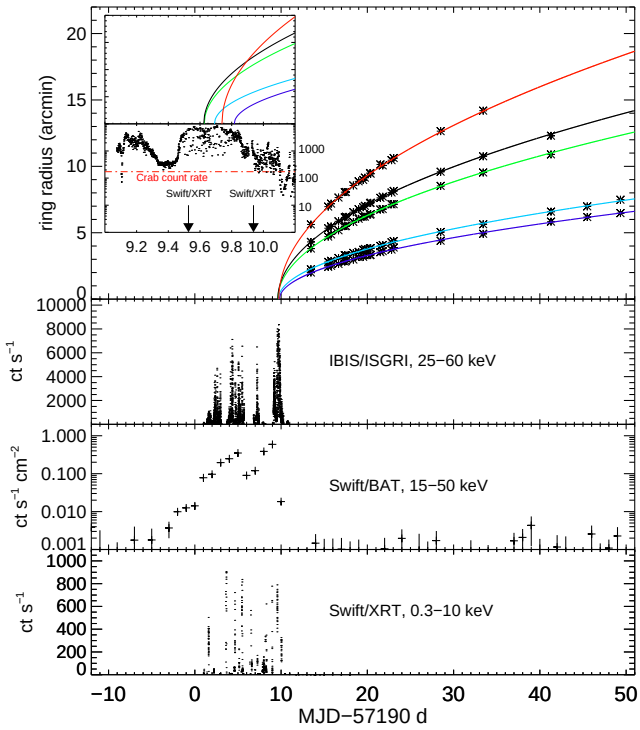

Figure 4. The bottom three panels show (from bottom to top): the 60 s binned *Swift*/XRT (0.3-10 keV) light curve, the daily binned *Swift*/BAT X-ray light curve at 15-50 keV based on the results from the BAT transient monitor (Krimm et al. 2013), and the INTEGRAL/ISGRI light-curve at 25-60 keV (see text, Rodriguez et al. 2015a; Kuulkers 2015). Top panel: Expansion of the five dust rings detected by *Swift*/XRT (symbols) along with the best-fit model (solid lines) given by eq. (3). The positional uncertainties of the rings are smaller than the size of the asterisk symbol used in this graphics and thus are not plotted. A close-up at the period of a major outburst detected by INTEGRAL/ISGRI (~ MJD 57199.7) is shown in the inset plot. The arrows denote the dates of simultaneous observations with *Swift*/XRT, while the horizontal dashed line corresponds to the count rate of Crab.

cannot account for all the details of the respective radial profile. For example, the poor global fits of observations #1 and #2 (see Figs. 3 and B1, respectively) are mainly caused by the difference between the data and the model at large angular distances (i.e., $\theta \gtrsim 350''$ and $450''$, respectively). The observed excess of emission, with respect to the predicted one by the fifth Lorentzian function (see Fig. 3), can be understood in terms of a diffuse X-ray scattered emission, which, if the photon statistics allow, can be observed as an X-ray halo (see also Fig. 2). This may be the result of dust layers having a finite width instead of being infinitely thin, as we assumed in our analysis for simplifying reasons. Other sources of the observed excess may be the X-ray scattered emission due to prior outburst activity (see §4.3) and/or multiple scatterings, although the latter are expected to be the least important source as discussed in §2.

Although the two-component model does not provide an overall good fit to some observations, it still allows for an accurate determination of the angular size of the rings. This argument is also *a posteriori* supported by the fitting results of the ring expansion, which are summarized in Tab. 1 and Fig. 4.

The results in Tab. 1 support the hypothesis of a single outburst of short duration occurring at t_0 that is being scattered by dust clouds of small width, i.e. dust layers or screens, located at different locations between the observer and the source. Henceforth, we adopt the following convention: the dust layer responsible for the detection of the ring i will be labeled as the "dust cloud i". The best-fit value for t_0 suggests that an X-ray outburst of short duration should have taken place at MJD = 57190 + t_0 ~ 57199.75, namely ~ 3.7 days before the first detection of the X-ray rings. Figure 4 (top panel) shows that the expansion of the rings follows the theoretical prediction, i.e. $\theta \propto \sqrt{\Delta t}$, where Δt is the time delay since the outburst. At late times the angular size of the outer rings (3-5) is larger than the *Swift*/XRT FOV, which also explains the lack of data points in the respective model curves in Fig. 4. Interestingly,

a broad X-ray flare with its peak centered at ∼MJD 57199.7 has been detected in both soft[5] and hard X-rays, i.e. in 0.3-10 keV with *Swift*/XRT, in 15-50 keV with *Swift*/BAT (BAT transient monitor, Krimm et al. 2013), and 25-60 keV with INTEGRAL IBIS/ISGRI. The respective light curves are also shown in Fig. 4.

A close-up to the time-interval of the X-ray outburst as detected by INTEGRAL IBIS/ISGRI is shown in the inset of the top panel in Fig. 4. The arrows denote the dates were simultaneous *Swift*/XRT observations are available, while the horizontal dashed line corresponds to the Crab count rate (172.1±5.6 ct s^{-1}) as measured by INTEGRAL IBIS/ISGRI during satellite revolution 1528; it is noteworthy that the X-ray flux during this burst corresponds to the highest flux observed by INTEGRAL after the trigger of the V404 Cyg activity. Although the outburst has a duration of $\delta t \sim 0.9$ days, this is still short enough compared to the time delay of the first X-ray ring detection, as to make the δ-function approximation of the X-ray outburst valid (see also §2). In any case, the derived value for t_0 coincides (within the errors) with the INTEGRAL/ISGRI outburst period.

Fixing $t_0 = 57199.75$ d and performing a one-parameter fit to the ring expansion using eq. (3), we derived the distances of the dust layers. These fall in the range ∼1.2-2.1 kpc from the observer with the most distant one being located close to the source and producing the innermost X-ray rings. The calculated errors to the distances are dominated by the error of the source distance itself ($d = 2.39 \pm 0.14$), while the 1σ statistical errors derived from the fit of the ring expansion are approximately one order of magnitude smaller (see Tab. 1). We found that the spatial separation of the dust clouds that produce the two innermost X-ray rings is small, i.e. ∼ 0.07 kpc. This is in agreement with their observed angular proximity (see e.g. Figs. 2 and 3) and points towards a common origin of their dust content. If we were to relax the assumption of infinitely thin dust layers, our results would suggest the presence of one dust cloud at a distance ∼ 2 kpc, with a finite width of ∼ 100 pc and a non-uniform density that peaks roughly at the positions x_1 and x_2. For the width estimation, we used the FWHM of the first two Lorentzian functions, as derived from modeling the radial profile of the first *Swift*/XRT observation. Similar conclusions can be drawn for the clouds 3 and 4.

The distances that we derived can be then compared with other indirect measurements of the dust distribution in the direction of V404 Cyg, such as measurements of the extinction A_λ. We choose, in particular, the three-dimensional extinction maps based on IPHAS photometry (Sale et al. 2014) and plot in Fig. 5 the extinction A_λ vs. the distance from the observer in the direction of V404 Cyg (black histogram). The vertical dotted lines denote the position of the dust layers as derived by modeling the ring expansion and the width corresponds to the total error. Similar color coding as in Fig. 4 has been used.

In the direction of V404 Cyg the extinction is relatively low, except for a peak at ∼ 0.85 kpc, where $A_\lambda \simeq 1.2$. The positions of the dust layers fall into regions where $A_\lambda \sim 0.1 - 0.2$. However, we find no dust layer located at the distance of maximum extinction. An X-ray ring produced by scattering on a hypothetical dust layer located at ∼ 0.85 kpc and detected simultaneously with the other five rings on MJD 57205.5 should have an angular size of ∼ 9′ (see eq. (3)). The *Swift*/XRT image, however, shows no signs of an additional ring with that angular size (see white circle in Fig. 2). Since

[5] Henceforth, we will refer to the 0.3-10 keV energy band of *Swift*/XRT as the "soft" X-ray band, unless stated otherwise.

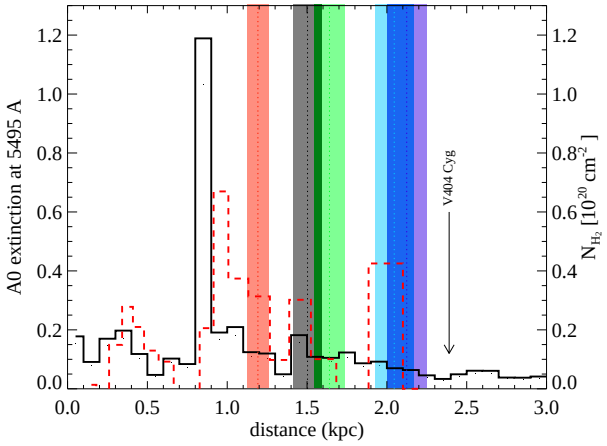

Figure 5. The extinction A_λ as a function of distance from the observer in the direction of V404 Cyg (black lines). The data are obtained from three-dimensional extinction maps based on IPHAS photometry (Sale et al. 2014). The distribution of N_{H_2} (red dashed lines) as derived from CO measurements in the direction of V404 Cyg (Dame et al. 2001), using the Galactic rotation curve by (Clemens 1985) for $R_\odot = 8.5$ kpc and $V_\odot = 220$ km/s, is also shown. The inferred distances of the dust layers are marked with dotted vertical lines, while the width of the colored bars denotes the total error. Same color coding as in Fig. 4 is used.

the hypothetical ring should fall within the FOV of *Swift*/XRT, the absence of a dust-scattered ring in combination with the high extinction value might imply a very small scattering cross section (see e.g. eq. (4)). Since we observe no ring structure even at $E = 1$ keV, we may estimate a lower limit of the average grain size of a hypothetical dust cloud located at 0.85 kpc. Substitution of $\theta = 9'$ and $E = 1$ keV in eq. (5) results in $\alpha \gg 0.11\,\mu$m, which translates to $\alpha_{\rm max} \gg 0.18\,\mu$m for $q = 3.5$ (see eq. (11)).

In addition, we compared the derived distances with the distribution of molecular hydrogen (H_2) in the direction of V404 Cyg as derived by CO measurements. For this, we used the data from the Galaxy CO survey (Dame et al. 2001), and, in particular, the velocity-resolved, moment-masked (i.e., noise-suppresed) (Dame 2011) radio maps of the Individual Survey DHT18 (Second Quadrant, $1/4^o$ sampled). For the de-projection of the observed velocities we used the rotation curve of Clemens (1985) for $V_\odot = 220$ km/s and $R_\odot = 8.5$ kpc. The latter is close to the value derived by recent dynamic studies of the Galactic center (Chatzopoulos et al. 2015), namely $R_\odot = 8.33 \pm 0.11$. The distribution of N_{H_2} (in cm^{-2}) is over plotted in Fig. 5 with a red dashed line. The derived distances of the five dust layers seem to coincide with those where the column density appears enhanced. The maximum column density ($\sim 6 \times 10^{19}$ cm^{-2}) is found at a distance close to the maximum extinction A_λ, where no dust cloud is inferred from the *Swift*/XRT observations.

It is noteworthy that the distribution of N_{H_2} is very sensitive to the adopted values of the Galactic constants ($R_\odot$,$V_\odot$) and of the Galactic rotation curve itself (see e.g. Clemens 1985; Sofue et al. 2009; Bhattacharjee et al. 2014). This is illustrated in Fig. 6, where we plot the derived distribution of N_{H_2} using three different values of Galactic constants, namely ($R_\odot$ kpc,$V_\odot$ km/s)=[(8.5, 220), (8.5, 225), (8.8, 275)]. For the first pair of values (black line), the Galactic rotation curve by Clemens (1985) was used, while the rotation curve by Brand & Blitz (1993)

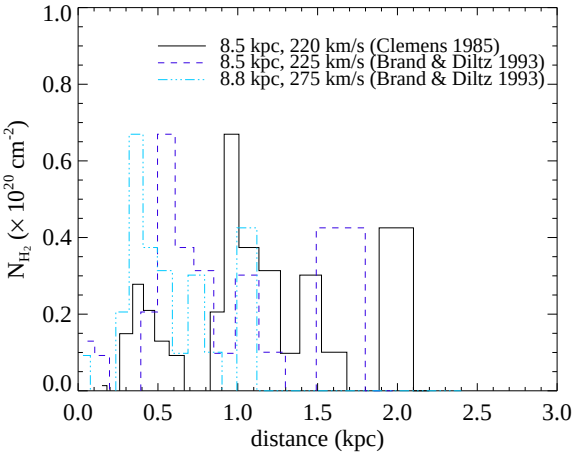

Figure 6. The distribution of molecular hydrogen in the direction of V404 Cyg as inferred from the same CO radio maps but for different values of the Galactic constants and Galactic rotation curves (see inset legend).

was adopted for the other two (cyan dashed-dotted and blue dashed lines).

In summary, we have showed that the angular structure of the *Swift*/XRT images can be adequately explained by scattering of a short duration X-ray outburst on dust layers located at distances $\gtrsim$ 1.2 kpc from the observer. These conclusions are independent of the composition and properties of the dust, which will be determined in the following section.

4.2 Properties of the dust clouds

To model the evolution of the specific scattered flux of the X-ray rings, we assumed that the grain size distribution in all five clouds is described by a generalized Mathis-Rumpl-Nordsieck (MRN) model (Mathis et al. 1977):

$$n(\bar{\alpha}) = A\bar{\alpha}^{-q} H[\bar{\alpha} - \bar{\alpha}_{\rm min}] H[\bar{\alpha}_{\rm max} - \bar{\alpha}], \quad (13)$$

where $\bar{\alpha} \equiv \alpha/1\ \mu$m and $H[x]$ is the Heaviside function defined to be equal to 1 for $x > 0$ and to 0, otherwise. The model has four free parameters, namely the slope q, the normalization A, the minimum $\bar{\alpha}_{\rm min}$ and maximum $\bar{\alpha}_{\rm max}$ grain sizes. The normalization A (dimensionless) is related to the total number of grains in a given cloud through $N_{\rm tot} = \int d\bar{\alpha} n(\bar{\alpha}) = A\left(\bar{\alpha}_{\rm max}^{1-q} - \bar{\alpha}_{\rm min}^{1-q}\right)/(1-q)$. In the following, we assume that the model parameters are different among the dust clouds. Substitution of the power-law distribution in eq. (9) results in

$$F_{\rm sc,i}(\theta, E) = \mathcal{F}_{\rm X}^{(i)}(E) \int_{\bar{\alpha}_{\rm min}}^{\bar{\alpha}_{\rm max}} d\bar{\alpha}\, \bar{\alpha}^{6-q} \exp\left(-\frac{\theta^2}{2(1-x_i)^2\Theta^2(E,\bar{\alpha})}\right), \quad (14)$$

where we used the approximation $\theta_{\rm sc} \approx \theta/(1-x_i)$ and the normalization is given by

$$\mathcal{F}_{\rm X}^{(i)}(E) = 2.54 \times 10^{-11} \frac{\Phi_{\rm X}(E) N_{\rm H,i} A_{\rm i} C_{\rm d,i}(E)}{x_{\rm i}(1-x_{\rm i})}, \quad (15)$$

where $\mathcal{F}_{\rm X}^{(i)}$ is in units of erg cm^{-2} s^{-1} keV^{-1} and $N_{\rm d} \equiv N_{\rm H,i} A_{\rm i}$ is the column density of dust, that is the number of grains per cm^2. In principle, by fitting the scattered flux of the individual rings as given by eq. (14), the following parameters of the dust clouds can be determined: q, $\bar{\alpha}_{\rm min}$,$\bar{\alpha}_{\rm min}$ and $\mathcal{F}_{\rm X}(E)$. Due to the angular proximity of the rings 1-2 and 3-4 (see also §3), the use of the flux profile extracted from individual rings is less reliable (see e.g. Tiengo et al. 2010). For the purposes of the fit, we therefore used the cumulative scattered flux of rings 1-2 and 3-4, assuming that the dust properties of the the clouds that are responsible for the formation of adjacent X-ray rings are the same. This assumption is also justified by the proximity of the dust clouds 1-2 and 3-4, as it was derived in §4.1 by modelling the ring expansion (see also Tab. 1). From this point on, we will treat the innermost rings as one, with an angular size given by the mean of the angular sizes of the rings 1 and 2. In addition, in eq. (14) we substitute $x_{\rm i}$ by the mean of the distances, i.e. $\langle x \rangle_{12} = (x_1 + x_2)/2$. The same applies for the third and fourth rings.

For each individual ring, we jointly fitted $F_{\rm sc,i}(\theta, E)$ at four different energies using the expression (14). To account for the energy dependence of $\mathcal{F}_{\rm X}$, we allowed for four different normalizations. In total, the number of free parameters required for modelling one ring are seven: four related to the energy dependent-normalization plus three related to the grain size distribution (the fourth free parameter of the grain size distribution, A, is absorbed in the normalization).

For each ring, we first searched for the best-fit model after leaving free all the model parameters. We imposed, however, limits on both $\alpha_{\rm min}$ and $\alpha_{\rm max}$. These were respectively bounded in the ranges 10^{-5}–$0.1\,\mu$m and 0.1–$0.5\,\mu$m. We caution the reader that our results regarding the largest grains should be trusted up to $\sim 0.3\,\mu$m, given that for larger grains the RG approximation overestimates by at least a factor of $\sim 3-4$ (e.g. Smith & Dwek 1998) the scattered flux of X-ray photons with energy $E \sim 1$ keV (see also §5 for a relevant discussion).

Figure 7 shows the angular profile of the scattered flux for rings 1-2 (left panel), rings 3-4 (middle panel) and ring 5 (right panel) at four different energies (coloured symbols) along with the best-fit model (solid lines). The respective parameter values are listed in Table 2. To facilitate a comparison among the rings, the specific scattered flux of the rings is also shown in Fig. 8. The fact that the profiles of rings 3-4 and ring 5 are almost overlapping does not necessarily mean that the corresponding dust layers have the same hydrogen column density, since the dust cloud 5 is located closer to the observer (see also below). The intensity profiles of all rings, except for the outermost, show no evidence of an exponential cutoff, which could strongly constrain the minimum size of the grains (see §2). *Swift*/XRT observations of the innermost rings after MJD 57239.3 (observation #21) could shed light on the actual size of the smallest grains. However, the signal-to-noise ratio of follow-up observations was not high enough (time exposure $\lesssim$ 1ks) for a reliable spectral extraction and fitting. We note that the data at 2.5 keV show systematically a larger scatter, which is due to a deficit of photons at the higher energy part of the spectrum.

As a second step, we created a grid of values for two model parameters, namely $\alpha_{\rm min} - \alpha_{\rm max}$ and $q - \alpha_{\rm max}$. Based on the χ^2 value of the fits, the 1σ, 2σ and 3σ significance levels were then computed and the contour plots for $\alpha_{\rm min} - \alpha_{\rm max}$ and $\alpha_{\rm max} - q$ were produced. These are presented in Fig. 9 for rings 1-2 (left column), rings 3-4 (middle column), and ring 5 (right column). A few things worth mentioning follow:

- Rings 1-2: only a lower limit on the maximum grain size ($\alpha_{\rm max} \gtrsim 0.15\,\mu$m) can be determined. This is to be expected, since the *Swift*/XRT data show no evidence of a flat angular profile at $\theta \lesssim 2'$ (see also §2). Moreover, a minimum grain size larger than $\sim 4 \times 10^{-3}\,\mu$m can be already excluded at a 3σ level. The power-law index of the size distribution can be constrained though, with a best-fit value $q = 4.42 \pm 0.02$.
- Rings 3-4: in contrast to the most distant dust clouds, for the

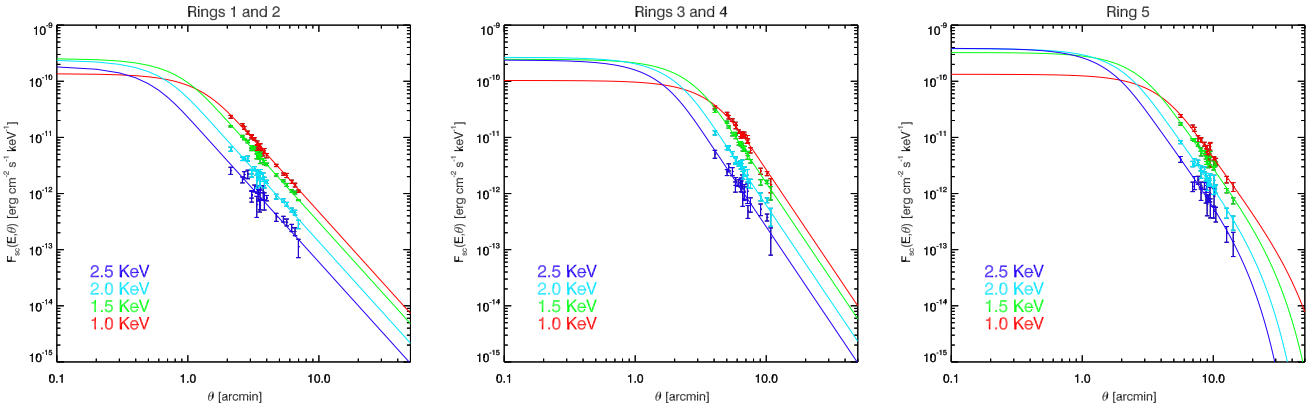

Figure 7. Scattered flux of the X-ray rings as a function of the observed angular size θ for different energies marked on the plot. The cumulative profiles of the two innermost rings and rings 3-4 are shown in the left and middle panels, respectively. The flux profile of the outermost ring is plotted in the right panel. For the cumulative profiles, we used the average angular size of the two adjacent rings. The best-fit model is plotted in all panels with a solid line.

Table 2. Best-fit values derived by modelling the radial profile of the X-ray scattered flux at four different energies.

Ring(s)	$\alpha_{\rm min}$ [μm]	$\alpha_{\rm max}$ [μm]	q	$\langle\alpha\rangle$ [μm]	$\mathcal{F}_{\rm X}$(1keV)	$\mathcal{F}_{\rm X}$(1.5keV)	$\mathcal{F}_{\rm X}$(2keV)	$\mathcal{F}_{\rm X}$(2.5keV)	$\chi^2_{\rm red}$ (dof)
					[erg cm^{-2} s^{-1} keV^{-1}]				
1-2	$10^{-5}\pm$N/A[a]	0.18 ± 0.03	4.42 ± 0.02	0.07 ± 0.01	$(3.0 \pm 0.2) \times 10^{-8}$	$(5.5 \pm 0.3) \times 10^{-8}$	$(5.2 \pm 0.3) \times 10^{-8}$	$(4.0 \pm 0.3) \times 10^{-8}$	1.90(81)
3-4	$10^{-5}\pm$N/A[a]	0.17 ± 0.01	3.53 ± 0.06	0.10 ± 0.01	$(1.8 \pm 0.3) \times 10^{-7}$	$(4.3 \pm 0.8) \times 10^{-7}$	$(4.7 \pm 0.9) \times 10^{-7}$	$(4.2 \pm 0.9) \times 10^{-7}$	1.91(70)
5	0.02 ± 0.01	0.24 ± 0.03	3.77 ± 0.11	0.13 ± 0.02	$(4.2 \pm 1.1) \times 10^{-8}$	$(1.0 \pm 0.3) \times 10^{-7}$	$(1.2 \pm 0.3) \times 10^{-7}$	$(1.2 \pm 0.4) \times 10^{-7}$	1.89(65)

a As the best-fit is obtained for a value equal to the imposed lower bound, the error calculation is not applicable in this case.

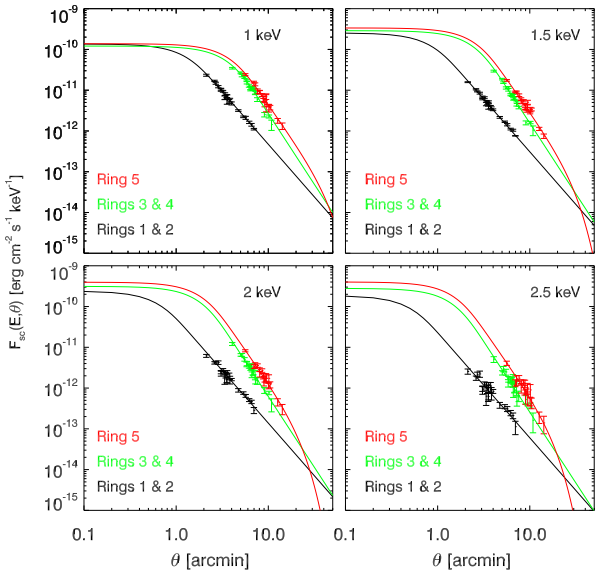

Figure 8. Comparison of the intensity angular profiles of the X-ray rings at fixed energies.

dust clouds 3 and 4 we can constrain both $\alpha_{\rm max}$ and q at a 3σ level. The best-fit value of the former is compatible with the lower limit of $\alpha_{\rm max}$ derived from rings 1-2, whereas the grain size distribution in clouds 3 and 4 is best described by a shallower power-law with $q \sim 3.5$. No lower limit can be found for the minimum grain size, yet the data of rings 3-4 exclude values larger than $\sim 0.017\,\mu$m at a 3σ level.

- Ring 5: the angular profile of the specific intensity shows hints of an exponential steepening at large angles ($\gtrsim 10'$), which is imprinted on the contour plot of $\alpha_{\rm min}$ and $\alpha_{\rm max}$ (top panel on the right). At the 1σ level we find a narrow range of values for $\alpha_{\rm min}$ (0.01-0.025 μm). At the 3σ level, however, only an upper limit on the size of small grains can be imposed, i.e. $\alpha_{\rm min} \lesssim 0.03\,\mu$m. Similar conclusions can be drawn for $\alpha_{\rm max}$. The largest grains cannot be smaller than $0.2\,\mu$m, in agreement with the other dust clouds. Finally, the power-law index of the size distribution is constrained at the 3σ level in the range $3.5 - 4.0$.

From the best-fit values of the normalization at a fixed energy, we can obtain the ratios of the hydrogen column densities for different dust layers, such as:

$$\frac{N_{\rm H,12}}{N_{\rm H,5}} \approx \frac{\mathcal{F}_{\rm X}^{(12)}(E)}{\mathcal{F}_{\rm X}^{(5)}(E)} \frac{(1-\langle x\rangle_{12})\,\langle x\rangle_{12}}{(1-x_5)\,x_5}, \tag{16}$$

where we assumed that the number of grains per hydrogen atom is the same in all clouds and dropped the factor $C_{\rm d,i}$, since this is not sensitive to the grain composition (Mauche & Gorenstein 1986) (see also §2). In the above, $N_{\rm H,12}$ represents the average column density of dust clouds 1 and 2. As already mentioned in §4.1 and later in §4.3, these are most probably one dust cloud of finite width, whose average column density we are probing. Having derived the ratios at four different energies, we calculated the weighted means, namely $N_{\rm H,12}/N_{\rm H,5} = 0.19 \pm 0.03$, $N_{\rm H,12}/N_{\rm H,34} = 0.059 \pm 0.006$, and $N_{\rm H,34}/N_{\rm H,5} = 3.5 \pm 0.6$. Thus, the intermediate dust clouds have the highest column density. This is 3.5 times higher than that

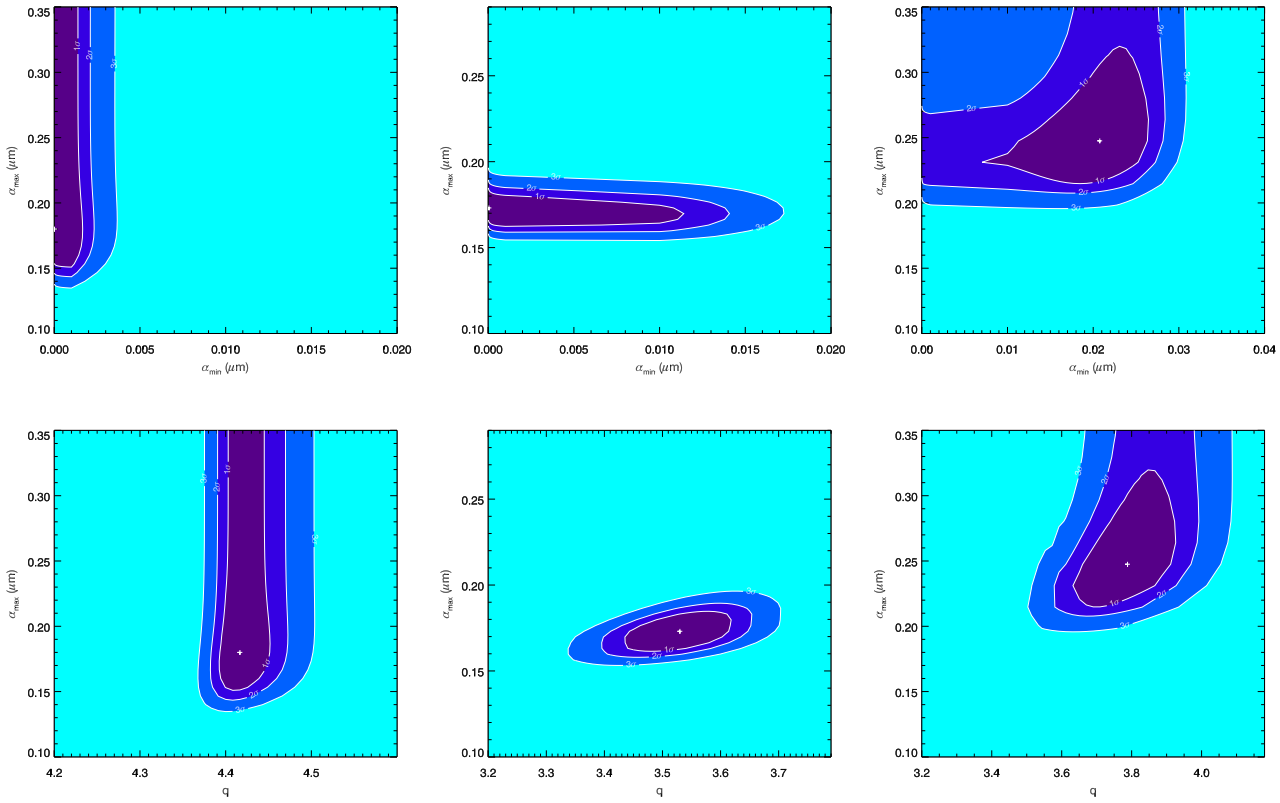

Figure 9. Contour plots for two model parameters (top row: $\alpha_{\rm min} - \alpha_{\rm max}$; bottom row $\alpha_{\rm max} - q$) as derived by jointly fitting at four different energies the scattered flux of the rings 1-2 (left column), rings 3-4 (middle column) and ring 5 (right column). The lines mark the 1σ, 2σ and 3σ confidence levels. In all cases, the best-fit value is marked with a cross.

of the fifth dust cloud, which may also explain the approximately equal intensities of rings 3-4 and 5, given their different distances from the observer. Interestingly, the column density of the clouds located closest to V404 Cyg is $\sim 6\% N_{\rm H,34}$. These findings are in rough qualitative agreement with the extinction histogram shown in Fig. 5, where the lowest extinction values are found at distances $\gtrsim 2$ kpc, i.e. where the dust layers 1 and 2 are located. Quantitatively, we find that the ratios $N_{\rm H,34}/N_{\rm H,5}$ and $N_{\rm H,34}/N_{\rm H,12}$ as derived from the extinction maps (Sale et al. 2014) are by a factor of ~ 3 smaller than our estimates, while the $N_{\rm H,12}/N_{\rm H,5}$ ratio is the same (within uncertainty values). This implies that our analysis is overestimating the $N_{\rm H,34}$ column density by a factor of ~ 3. A simple explanation for this difference is that the dust-to-hydrogen ratio is not the same for all clouds as originally assumed in our calculations (the $A_{\rm i}/A_{\rm j}$ term has dropped from the l.h.s. of eq. (16)). In any case, the ratio of the normalizations $\mathcal{F}_{\rm X}^{(i)}$ can be directly related to the ratio of dust column densities $N_{\rm H,i}A_{\rm i}$ without resorting to any additional assumptions.

4.3 Effects of the X-ray activity since MJD 57188.5

In contrast to other studies of dust scattered X-ray emission, where the source may exhibit one major outburst (see e.g. Vaughan et al. 2004; Vianello et al. 2007), the LMXB V404 Cyg entered a new period of enhanced activity on MJD 57188.5 and, since then, it exhibited multiple X-ray flares in both soft and hard energy bands (Motta et al. 2015; Ferrigno et al. 2015; Rodriguez et al. 2015b; Segreto et al. 2015). In summary,

- during MJD 57188.5-57191.0 no significant flares were detected by either *Swift*/BAT or *Swift*/XRT.
- multiple flares have been detected in the period of MJD 57191-57198 with the count rate reaching a maximum on MJD 57194 (see e.g. Fig. 4 and Rodriguez et al. (2015a)).
- finally, on ~MJD 57199.7, a major outburst that lasted approximately $\sim$ 0.9 d, was detected by all observing instruments. Interestingly, its fluence in 25-60 keV is approximately equal to the fluence measured by INTEGRAL/ISGRI over the whole period between MJD 57191 and MJD 57198.

This preceding X-ray outburst activity may be imprinted on the angular profiles shown in Fig. 3, which can be understood as follows. The simultaneous observation of X-ray rings due to the scattering of a single outburst from dust layers located at different distances from the observer implies that the scattered photons should travel along paths of the same length, i.e. the scattering points on the dust layers should belong to an ellipse. This is illustrated in Fig. 10, where two ellipses corresponding to different time-delays are shown. The colored regions denote the dust layers where the X-ray scattering takes place, with the color gradient mimicking the gradient of the column density. Here, the inclination of the dust layers with respect to the LOS has been arbitrarily chosen to be 90°. Notice that the scattered emission of a prior outburst at $t_0' < t_0$ (blue line) by the dust layer at distance x_1 could "contaminate" the scattered emission observed, at the same angle, but caused by

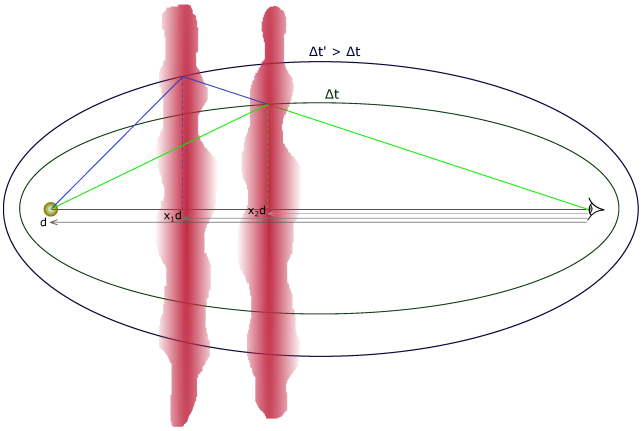

Figure 10. An illustration of the locus of points determined by scattering events on dust screens (colored regions) located at different distances from the observer. The inner and outer ellipses correspond to different time delays marked on the plot. The colored solid lines show the travel paths of photons that are: (i) scattered by different dust layers, (ii) emitted during source outbursts at $t_0' < t_0$ (blue line) and t_0 (green line) and (iii) detected simultaneously with the same observed angle.

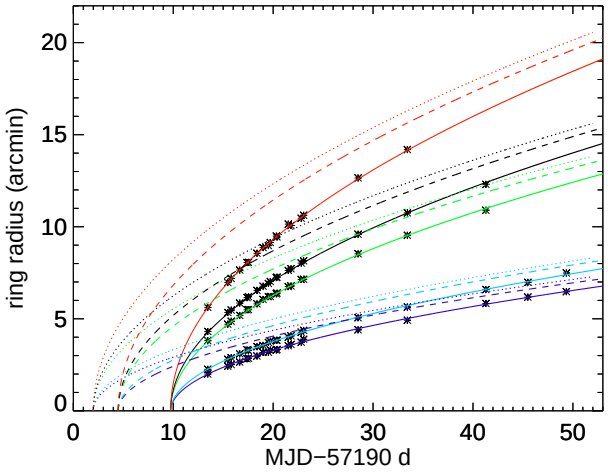

Figure 11. Expansion of dust scattered rings for three bursts occurring at different times: t_0=MJD 57199.75 (solid lines), MJD 57194.5 (dashed lines), and MJD 57192.0 (dotted lines). The *Swift*/XRT observations are plotted with asterisks. The earlier burst represents the start of the enhanced activity of V404 Cyg, while the latest major burst is the one responsible for the *Swift*/XRT detection of the rings.

the scattering of an outburst at t_0 on the dust layer at distance x_2 (green line). Thus, the X-ray scattering from bursts occurring before t_0 =57199.75 could be imprinted on the angular profile of the rings shown in Fig. 3.

Having derived the distances of the dust layers by modeling the ring expansion due to the latest, major outburst on t_0 = 57199.75 d, we may estimate the expansion of ring-like structures caused by the earlier activity of V404 Cyg described above. This is illustrated in Fig. 11, where the expansion of dust scattered rings due to outbursts on t_0 =MJD 57194.5 and 57192.0 are shown with dashed and dotted lines, respectively. In all cases, the angular region enclosed by the solid and dotted lines corresponds to a maximum "region of influence" from bursts taking place after the onset of the V404 Cyg activity. All the *Swift*/XRT observations of the innermost rings (blue and cyan lines) are affected by the previously scattered emission on the most distant clouds. Similarly, the third and fourth rings (green and black lines) are predominantly affected by previous bursts that were scattered on the dust clouds 3 and 4. The contamination becomes important after MJD 57210. Finally, the outermost ring (red lines) is mostly contaminated by the scattered emission on the dust clouds 3 and 4. Interestingly, the last two *Swift*/XRT detections of the outermost ring are the least affected by prior scattered emission.

A question that naturally arises is whether the earlier X-ray activity of the source could give rise to distinct ring-like structures similar to the detected ones. To answer this question one has to estimate the contamination of the previous bursts in the dust scattered rings of the final burst (MJD 57199-57200). We proceed with some simple estimations for the ratio of the fluence in soft X-rays (0.3-10 keV) during and before the burst ($R_{\rm fl}$). Since the system is highly variable an accurate measurement of the fluence in soft X-rays would require a continuous monitoring of the system, while the *Swift*/XRT observations cover the burst for small time intervals (typically ∼1-2 ks). However, we may estimate $R_{\rm fl}$ using the fluence in the 25-60 keV band as measured by INTEGRAL IBIS/ISGRI during the same intervals, assuming a correlation between soft and hard X-rays. Between MJD 57191 and MJD 57198 the system was observed with INTEGRAL IBIS/ISGRI for ∼5.1 d, while during the major burst the system was continuously monitored (∼1 day exposure time). Assuming that the average flux of V404 Cyg during the observing gaps was similar to the observed one, we estimated that ∼39% of the exposure corrected fluence of the system was emitted after MJD 57199. In addition, we found that the average flux during the major burst increased by a factor of ∼ 5 compared to the average flux prior to it. In this first period of enhanced X-ray activity (MJD 57191-57198), multiple strong bursts spanning over one-day intervals, i.e. MJD 57193.6-57194.5 and MJD 57194.6-57195.7, can be identified (see also Fig. 4). Yet, the respective fluences were estimated to be ∼31% of the fluence during the major burst; the same applies for the fluxes. These estimates can be extended to the soft X-ray band under the former assumptions (i.e., correlated soft and hard X-ray emission).

As the estimated fluence of the strongest earlier outbursts was by a factor of ∼ 3 less than that of the major outburst, these would probably not give rise to distinct ring-like structures similar to the detected ones. What is observed as "bridge" emission between the peak positions of successive rings (see Fig. 3) could be the result of previous scatterings though. The signatures of the strongest earlier bursts to the total angular profile should appear as small-amplitude peaks over a diffuse emission component (halo). Interestingly, the appearance of spiky features between the successive major peaks at late times (with respect to t_0) could also be explained as a residual of prior X-ray activity; see e.g. observations #10 and #11 in Fig. B1. If this is the case, their evolution in time should also scale as $\sqrt{\Delta t}$. We finally note that no significant deviations from the rings expansion law $\theta \propto \sqrt{\Delta t}$ are expected as long as the respective peaks in the angular profile can be securely distinguished from the bridge emission. For the spectral analysis of the X-ray rings we selected part of the bridge emission as the background in order to minimize the effect of the previously scattered emission.

5 DISCUSSION

Our analysis was based on the RG approximation for the scattering cross section, which turns out to be insufficient for describing

the scattering process of < 1 keV photons by μm-sized grains. We therefore restricted the fitting of the scattered X-ray flux and the subsequent analysis to energies $\geqslant 1$ keV. Although at 1 keV the RG approximation is marginally valid, the scattered flux at this energy was included in the analysis, since the available data points for the spectral fitting were already sparse; the dust rings are practically not detected above 2.5 keV (see also Fig. 2). Our fitting results regarding the dust properties, and especially, the column densities could therefore differ from those obtained using the Mie expression for the scattering cross section, which adequately describes the process at sub-keV energies. To investigate the error introduced in our results, we repeated the fitting procedure of $F_{\rm sc}(E,\theta)$ after excluding the 1 keV energy bin, where the RG approximation becomes questionable. We find that the quality of the global fit remains the same (e.g. for rings 1-2, $\chi^2_{\rm red} = 1.95$ for 60 dof) and that the errors of individual parameters increase due to the smaller number of data points. The best-fit values of all parameters are the same as those listed in Tab. 2 within the 1σ errors. We also verified that this applies to the ratios of the column densities.

In addition, the difference between the RG approximation and the Mie solution at 1 keV for $\theta > 100''$ is expected to be small (see e.g. Smith & Dwek 1998; Corrales & Paerels 2015). Inspection of Fig. 6 in (Smith & Dwek 1998) shows that for $\theta = 100''$ and $E = 1$ keV, $I_{\rm sc}^{\rm (RG)}/I_{\rm sc}^{\rm (Mie)} \sim 2$ (3) for grains with sizes $a = 0.1\,\mu$m ($0.4\,\mu$m). Taking also into account that (i) the smallest angular size observed in the *Swift*/XRT data is $\theta = 2'$ and that (ii) the average size of dust grains we derived is $\sim 0.1\,\mu$m, we argue that our results would not differ significantly, if we were to perform the analysis using the Mie theory.

We showed that the *Swift*/XRT observations of the rings can be sufficiently explained by a generalized MRN model for the dust. Our results indicate that the largest grains in all clouds located along the LOS have similar sizes ($\sim 0.17 - 0.24\,\mu$m), while the average grain size, as defined by eq. (11) is $\sim 0.07 - 0.1\,\mu$m. The best-fit values for the maximum grain size suggest a dust composition of silicate (Mathis et al. 1977; Weingartner & Draine 2001). However, a composition with $\alpha_{\rm max} \sim 1\,\mu$m (e.g. graphite) cannot be excluded for the dust clouds 1-2 and 5, since $\alpha_{\rm max}$ is not limited from above. Regarding the minimum size of the grains, our results are compatible with $\alpha_{\rm min} \lesssim 0.004\,\mu$m (dust clouds 1-2) and $\lesssim 0.01\,\mu$m (dust clouds 3-4). Interestingly, the scattered flux profile of the fifth cloud showed hints of an exponential cutoff at large angles ($\theta \gtrsim 10'$). This, in turn, suggests that the minimum grain size in cloud 5 is typically larger than that inferred for the other clouds (see Fig. 9). The steepest grain size distribution is obtained for the most distant clouds, where q lies between 4.35 and 4.5 (at a 3σ CL). On the contrary, the power-law index of the size distribution in the intermediate clouds lies within the interval $3.4 - 3.7$, with the best-fit value being close to that of the MRN model (Mathis et al. 1977). The obtained size distribution in the fifth cloud is described by $3.6 \lesssim q \leqslant 4.2$, namely it is softer than the distribution in the intermediate clouds, yet harder than that in the most distant ones. These results suggest the presence of gradient in the dust properties along the LOS in the direction of V404 Cyg that requires further investigation.

By fitting the profiles of the X-ray scattered flux we were also able to determine the hydrogen column density ratios for different clouds (see eq. (15)). We showed that the intermediate clouds (at distance ~ 1.6 kpc) have the highest column density, which is by a factor of ~ 3.5 higher than that of the closest to us cloud. In contrast, the dust clouds that are located closer to V404 Cyg have the lowest column density, namely $\sim 6\%$ of $N_{\rm H,34}$. The above calculation was based on the assumption that the number of grains per hydrogen atom, $A_{\rm i}$, is the same in all clouds. We showed that the derived ratios are in qualitative agreement with those inferred from the extinction map in the direction of V404 Cyg (see Fig. 5). When viewed in a quantitative way, though, our results overestimate $N_{\rm H,34}$ by a factor or ~ 3. This incosistency could easily resolved, if the dust-to-hydrogen ratio in the intermediate clouds was larger than in the other clouds by the same factor.

In the more general case, where the dust-to-hydrogen ratio differs among the clouds, $A_{\rm i}$ can be deduced by eq. (15). This requires knowledge of the burst X-ray fluence $\Phi_{\rm X}(E)$ over the period of the major outburst (see Fig. 4) as well as of the hydrogen column density of each dust cloud $N_{\rm H,i}$. Both quantities can be roughly estimated as follows. The fluence in the *Swift*/XRT energy band was derived by assuming a correlation between soft (0.3-10 keV) and hard (25-60 keV) X-rays and by using the fluence measured by IBIS/ISGRI (see Sect. 4.3). Since the 3D extinction map in the direction of V404 Cyg is known, and the distances of the clouds were determined, the $N_{\rm H,i}$ can be derived using the relation between extinction $A_{\rm V}$ and hydrogen column density (e.g. Predehl & Schmitt 1995), i.e. $N_{\rm H} = (2.21 \pm 0.09) \times 10^{21}\, A_{\rm V}$ cm^{-2} (Güver & Özel 2009). The derived values for the number of grains per hydrogen atom in the clouds are $A_{12} = 10^{-13.9\pm0.2}$, $A_{34} = 10^{-13.2\pm0.4}$, and $A_5 = 10^{-13.9\pm0.5}$. The structure of a dust grain is complex as it is typically composed by many atoms or molecules (e.g. Weingartner & Draine 2001; Draine 2003). Yet, a zero-order estimation of total number of atoms contained in a dust grain can be made by comparing the characteristic sizes of atoms and grains. The average grain size as determined by our analysis is 0.1 μm, while the atomic sizes of C and Fe atoms are respectively $\sim 7 \times 10^{-5}$ μm and $\sim 14 \times 10^{-5}$ μm. Roughly speaking, a dust grain can be can be composed by $\sim 3.7 \times 10^9$ C atoms or $\sim 2.9 \times 10^8$ Fe atoms. Taking into account the $A_{\rm i}$ values we derived for the clouds, we estimate for the three dust clouds $\sim 1.2 \times 10^{16}$ C atoms cm^{-2} or $\sim 9.4 \times 10^{16}$ Fe atoms cm^{-2}. We remark that these values refer to the amount of metals contained in dust grains within the three clouds and not the gas in the ISM.

It is interesting that the tracers of atomic and molecular hydrogen become maximum at distances ~ 0.85 kpc, where no dust cloud is inferred from the *Swift*/XRT data (see Fig. 5). A fiducial dust cloud at the distance of ~ 0.85 kpc would produce an X-ray ring with angular size $\sim 9'$ on MJD 57205.5. As this would fall well within the *Swift*/XRT FOV (see Fig. 2), its absence should be related to the dust properties of the respective cloud. We estimated therefore that the maximum grain size should be $\gg 0.2\,\mu$m. A dust cloud composed by large grains ($\sim 1\,\mu$m) would suppress the scattered intensity even at 1 keV, while it would significantly attenuate X-rays at $\leqslant 0.5$ keV (e.g. Smith & Dwek 1998; Corrales & Paerels 2015). Alternatively, the absence of the X-ray ring might indicates a much smaller number of grains per hydrogen atom at ~ 0.85 kpc compared to the other clouds.

The analysis presented so far, as in most studies, does not take into account possible variations of the radial profiles in the azimuthal direction. We remind that the profiles shown in Figs. 3 and B1 were created by summing the counts of each annulus, i.e. integrating over the azimuthal angle. Although this method is sufficient for probing the average properties of the dust clouds, such as position and average column density, it cannot provide information about the spatial inhomogeneity of the dust clouds and/or their inclination with respect to the LOS. The photon statistics of the *Swift*/XRT observations are sufficient for quantifying the azimuthal variations of the ring intensity (see also Fig. 2). Figure 12 shows the

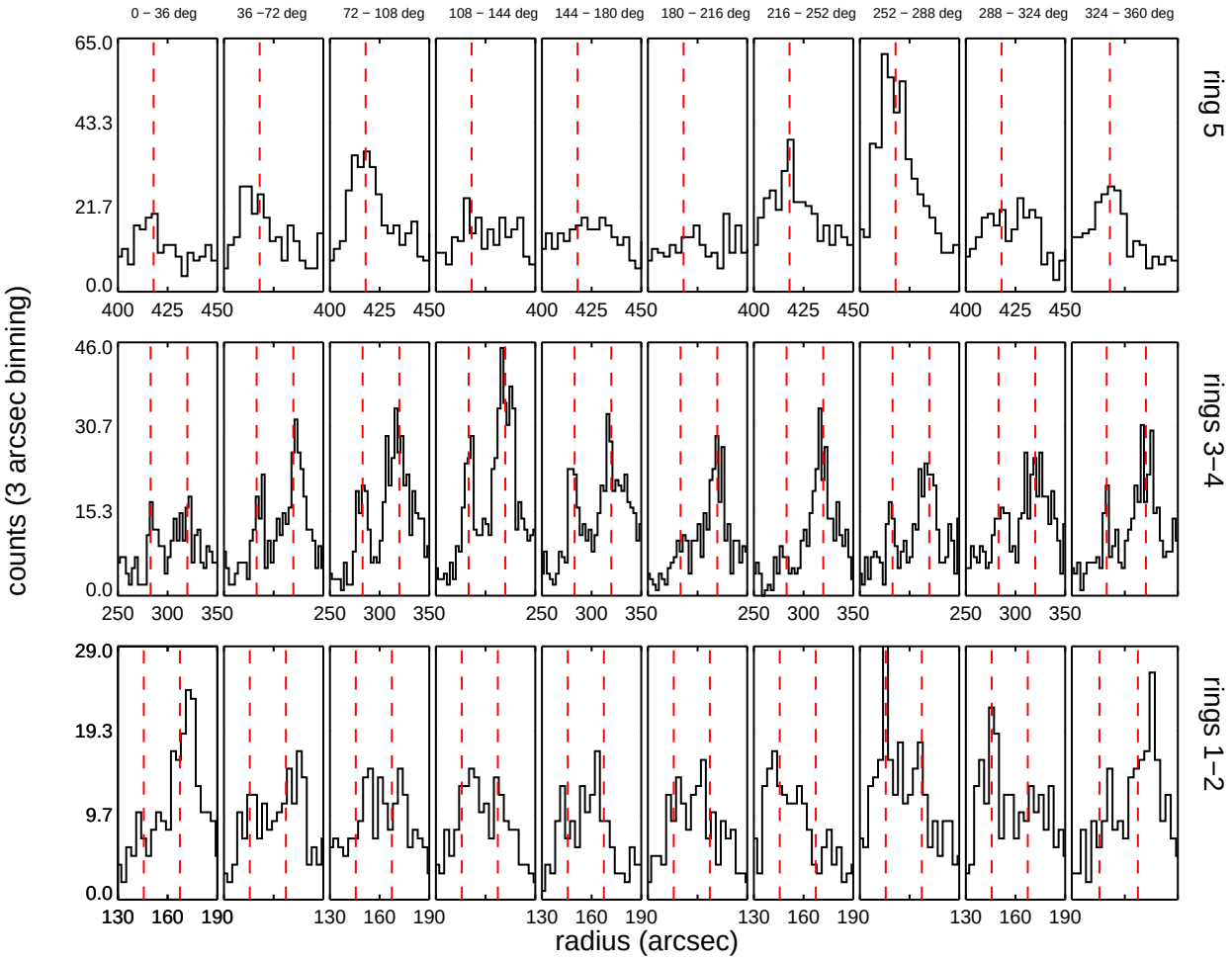

Figure 12. Variation of the radial profile of counts along the azimuthal direction for the *Swift*/XRT observation #2. The profiles have been created using a 36° bin in the azimuthal direction. The azimuth is measured counterclockwise, starting from the three o'clock ray (east direction) in Fig. 2. The profiles of the innermost, intermediate and outermost rings are plotted from bottom to top. The dashed red vertical lines denote the peak positions as derived by the analysis of the azimuthal integrated radial profiles.

azimuthal variation of the scattered photons for *Swift*/XRT observation #2. There are three important features that need to be mentioned: (i) the radial profile of ring 5 is highly variable along the azimuthal direction, with the peak number of counts changing by a factor of ∼5 above the background level (see sub-panels for 180°-216°and 252°-288°); (ii) azimuthal variations are also present in the rings 3 and 4, yet the variability amplitude is lower when compared to the ring 5. The peak number of counts of the fourth ring is for all azimuth angles larger compared to that of the third ring; (iii) the azimuthal behavior of the rings 1 and 2 is the most intriguing, as the second peak (corresponding to the ring 2) becomes prominent for azimuth angles 0°-36° and 324°-360° while the first peak dominates for azimuth angles of 216°-324°. Obviously, this information is lost from the azimuthal integrated radial profiles shown in Fig. 3. Similar features appear in all *Swift*/XRT observations with their significance varying according to the photon statistics of the observation.

The azimuthal variations are present in scales similar to the bin size of the azimuthal profiles, i.e. a few arcmin, yielding a projected distance of less than one pc for the location of the most distant clouds (∼ 2 kpc). These results imply a non-homogeneous matter distribution at sub-pc scales within the clouds, which could also lead to deviations from the theoretical prediction for the intensity profile $I_{\rm sc}(E,\theta)$. With a time-dependent study of the azimuthal profiles of the X-ray dust scattered rings, one could perform an X-ray tomography of the dust clouds at sub-pc scales. A more detailed study lies, however, outside the scope of the present paper.

6 SUMMARY

The scattered emission from bright X-ray point sources manifests itself often as an X-ray halo, while multiple (typically, one or two) X-ray rings can be detected if the X-ray source is variable, exhibiting short duration outbursts, and the dust along the LOS is not uniformly distributed but concentrated in discrete dust clouds. The recent *Swift*/XRT observations of multiple dust scattered X-ray rings from the LMXB V404 Cyg fall into the second category and offer a unique opportunity for studying the properties of dust along the LOS in the direction of V404 Cyg, for a number of reasons. Most

importantly, these are the first detections of dust scattered emission from the particular LMXB, whose distance is well constrained. Furthermore, the *Swift*/XRT observations span over a period of ~ 23 d (~ 36 d) for the outermost (innermost) ring(s) and allow for a time-dependent study of the X-ray scattered emission.

Using a simple but well proven theoretical framework, i.e. single X-ray scattering of a short X-ray impulse on discrete dust clouds along the LOS, we modeled the expansion of the dust scattered rings. We showed that these are produced by scattering of the last major outburst of V404 Cyg, on MJD 57199.7, that lasted ~ 0.9 d. The derived distances of the dust layers were found to be 2.12, 2.05, 1.63, 1.50 and 1.18 kpc from the observer. These positions coincide roughly with locations of enhanced extinction A_λ as determined by infrared photometry and of higher column densities of molecular hydrogen as derived by CO radio measurements. The spatial proximity of the most distant dust layers, as well as its azimuthal variation, implies the presence of one cloud with a finite width of ~ 100 pc located at $\sim$2 kpc; similar conclusions apply to the intermediate dust layers.

Assuming that the grain size distribution in all dust layers follows a power-law (i.e., a generalized Mathis-Rumpl-Nordsieck model), we fitted the angular profiles of the specific intensity at four different energies (1.0, 1.5, 2.0 and 2.5 keV) and derived the best-fit model parameters for the dust. In particular, we showed that the size distribution in the most distant cloud is significantly steeper ($q \sim 4.4$) than the distributions of the other clouds, which are described by $q \sim 3.4 - 3.7$. For the two intermediate dust layers we constrained, at a 3σ level, the maximum grain size in the range $0.16 - 0.20\,\mu$m, and set a lower limit at $\sim 0.18 - 0.2\,\mu$m for the other clouds. We can also exclude at a 3σ level that the smallest grains in the dust clouds 1-2, 3-4 and 5 have sizes $\alpha_{\rm min} \gtrsim 0.001\,\mu$m, $0.015\,\mu$m, and $0.03\,\mu$m, respectively. It is noteworthy that the angular intensity profile of the outermost X-ray ring showed hints of an exponential cutoff at large angles suggesting the presence of grains with $0.01 \leqslant \alpha_{\rm min} \leqslant 0.03\,\mu$m (at 1σ level). The best-fit values of the ratios of the dust column densities $N_{\rm d}$ between different clouds, i.e. $N_{\rm d,12}/N_{\rm d,5} = 0.19 \pm 0.03$, $N_{\rm d,12}/N_{\rm d,34} = 0.059 \pm 0.006$, and $N_{\rm d,34}/N_{\rm d,5} = 3.5 \pm 0.6$, indicate a higher $N_{\rm d}$ value at a distance ~ 1.6 kpc. Our results suggest the presence of a gradient in the properties of the dust in the direction of V404 Cyg that requires further investigation.

ACKNOWLEDGMENTS

We acknowledge the use of public data from the *Swift* data archive, which are a result of ToO observations from multiple PIs (D. Altamirano, A. P. Beardmore, M. Cadolle Bel, P. Gandhi, J. A. Kennea, E. Kuulkers, M. Middleton, S. Motta, R. M. Plotkin, J. Rodriguez, G. R. Sivakoff, G. Vasilopoulos), and we thank the *Swift* team for accepting and carefully scheduling the ToO observations. We thank the anonymous referee for useful comments that helped us to clarify subtle points and improve the manuscript. We also thank Dr. P. Predehl for useful discussions, Dr. S. Dimitrakoudis for providing Fig. 10 and Dr. R. Xue for helpful discussions on the use of CO radio maps. G. V. acknowledges support from the BMWi/DLR grants FKZ 50 OR 1208. M. P. acknowledges support from NASA through the Einstein Postdoctoral Fellowship grant number PF3 140113 awarded by the Chandra X-ray Center, which is operated by the Smithsonian Astrophysical Observatory for NASA under contract NAS8-03060.

REFERENCES

Arnaud K. A., 1996, in Astronomical Society of the Pacific Conference Series, Vol. 101, Astronomical Data Analysis Software and Systems V, Jacoby G. H., Barnes J., eds., p. 17
Beardmore A. P., Altamirano D., Kuulkers E., Motta S. E., Osborne J. P., Page K. L., Sivakoff G. R., Vaughan S. A., 2015, The Astronomer's Telegram, 7736, 1
Bhattacharjee P., Chaudhury S., Kundu S., 2014, Astrophysical Journal, 785, 63
Brand J., Blitz L., 1993, Astronomy & Astrophysics, 275, 67
Casares J., Charles P. A., 1994, Monthly Notices of the Royal Astronomical Society, 271, L5
Casares J., Charles P. A., Naylor T., 1992, Nature, 355, 614
Casares J., Charles P. A., Naylor T., Pavlenko E. P., 1993, Monthly Notices of the Royal Astronomical Society, 265, 834
Cash W., 1979, Astrophysical Journal, 228, 939
Chatzopoulos S., Fritz T. K., Gerhard O., Gillessen S., Wegg C., Genzel R., Pfuhl O., 2015, Monthly Notices of the Royal Astronomical Society, 447, 948
Clemens D. P., 1985, Astrophysical Journal, 295, 422
Corrales L. R., Paerels F., 2015, Monthly Notices of the Royal Astronomical Society, 453, 1121
Costantini E., Freyberg M. J., Predehl P., 2005, Astronomy & Astrophysics, 444, 187
Dame T. M., 2011, ArXiv e-prints:1101.1499
Dame T. M., Hartmann D., Thaddeus P., 2001, Astrophysical Journal, 547, 792
Dewey R., Mapes R., Reynolds T., 1969, Handbook of X-ray and Microprobe Data, Analytical chemistry. Pergamon Press
Draine B. T., 2003, Astrophysical Journal, 598, 1026
Draine B. T., 2011, Physics of the Interstellar and Intergalactic Medium
Draine B. T., Bond N. A., 2004, Astrophysical Journal, 617, 987
Draine B. T., Tan J. C., 2003, Astrophysical Journal, 594, 347
Ferrigno C. et al., 2015, The Astronomer's Telegram, 7662, 1
Garner A. et al., 2015, The Astronomer's Telegram, 7663, 1
Gazeas K., Vasilopoulos G., Petropoulou M., Sapountzis K., 2015, The Astronomer's Telegram, 7650, 1
Greiner J., Dennerl K., Predehl P., 1996, Astronomy & Astrophysics, 314, L21
Greiner J., Predehl P., Pohl M., 1995, Astronomy & Astrophysics, 297, L67
Güver T., Özel F., 2009, Monthly Notices of the Royal Astronomical Society, 400, 2050
Henke B. L., 1981, in American Institute of Physics Conference Series, Vol. 75, Low Energy X-ray Diagnostics, Attwood D. T., Henke B. L., eds., pp. 146–155
King A. L., Miller J. M., Raymond J., Reynolds M. T., Morningstar W., 2015, ArXiv e-prints
Klose S., 1994, Astrophysical Journal Letters, 423, L23
Kouveliotou C. et al., 2001, Astrophysical Journal Letters, 558, L47
Krimm H. A. et al., 2013, Astrophysical Journal Suppl. Ser., 209, 14
Kuulkers E., 2015, The Astronomer's Telegram, 7758, 1
Makino F., Wagner R. M., Starrfield S., Buie M. W., Bond H. E., Johnson J., Harrison T., Gehrz R. D., 1989, IAU Circ., 4786, 1
Mathis J. S., Lee C.-W., 1991, Astrophysical Journal, 376, 490
Mathis J. S., Rumpl W., Nordsieck K. H., 1977, Astrophysical Journal, 217, 425
Mauche C. W., Gorenstein P., 1986, Astrophysical Journal, 302,

371
Miller-Jones J. C. A., Jonker P. G., Dhawan V., Brisken W., Rupen M. P., Nelemans G., Gallo E., 2009, Astrophysical Journal Letters, 706, L230
Mooley K., Fender R., Anderson G., Staley T., Kuulkers E., Rumsey C., 2015, The Astronomer's Telegram, 7658, 1
Moretti A. et al., 2005, in Society of Photo-Optical Instrumentation Engineers (SPIE) Conference Series, Vol. 5898, UV, X-Ray, and Gamma-Ray Space Instrumentation for Astronomy XIV, Siegmund O. H. W., ed., pp. 360–368
Motta S., Beardmore A., Oates S., Sanna N. P. M. K. A., Kuulkers E., Kajava J., Sanchez-Fernanedz C., 2015, The Astronomer's Telegram, 7665, 1
Negoro H. et al., 2015, The Astronomer's Telegram, 7646, 1
Overbeck J. W., 1965, Astrophysical Journal, 141, 864
Predehl P., Burwitz V., Paerels F., Trümper J., 2000, Astronomy & Astrophysics, 357, L25
Predehl P., Klose S., 1996, Astronomy & Astrophysics, 306, 283
Predehl P., Schmitt J. H. M. M., 1995, Astronomy & Astrophysics, 293, 889
Richter G. A., 1989, Information Bulletin on Variable Stars, 3362, 1
Rodriguez J. et al., 2015a, Astronomy & Astrophysics, 581, L9
Rodriguez J. et al., 2015b, The Astronomer's Telegram, 7702, 1
Rolf D. P., 1983, Nature, 302, 46
Sale S. E. et al., 2014, Monthly Notices of the Royal Astronomical Society, 443, 2907
Segreto A., Del Santo M., D'Aí A., La Parola V., Cusumano G., Mineo T., Malzac J., 2015, The Astronomer's Telegram, 7755, 1
Shahbaz T., Bandyopadhyay R., Charles P. A., Naylor T., 1996, Monthly Notices of the Royal Astronomical Society, 282, 977
Smith R. K., Dame T. M., Costantini E., Predehl P., 2006, Astrophysical Journal, 648, 452
Smith R. K., Dwek E., 1998, Astrophysical Journal, 503, 831
Sofue Y., Honma M., Omodaka T., 2009, Publications of the Astronomical Society of Japan, 61, 227
Svirski G., Nakar E., Ofek E. O., 2011, Monthly Notices of the Royal Astronomical Society, 415, 2485
Tetarenko A., Sivakoff G. R., Gurwell M. A., Petitpas G., Wouterloot J. G. A., Miller-Jones J. C., 2015, The Astronomer's Telegram, 7661, 1
Tiengo A. et al., 2010, Astrophysical Journal, 710, 227
Trümper J., Schönfelder V., 1973, Astronomy & Astrophysics, 25, 445
van de Hulst H. C., 1957, Light Scattering by Small Particles
Vaughan S. et al., 2004, Astrophysical Journal Letters, 603, L5
Vianello G., Tiengo A., Mereghetti S., 2007, Astronomy & Astrophysics, 473, 423
Wagner R. M., Kreidl T. J., Howell S. B., Starrfield S. G., 1992, Astrophysical Journal Letters, 401, L97
Weingartner J. C., Draine B. T., 2001, Astrophysical Journal, 548, 296
Wilms J., Allen A., McCray R., 2000, Astrophysical Journal, 542, 914
Xiang J., Lee J. C., Nowak M. A., Wilms J., 2011, Astrophysical Journal, 738, 78
Życki P. T., Done C., Smith D. A., 1999, Monthly Notices of the Royal Astronomical Society, 309, 561

Table A1. X-ray observations log of V404 Cyg.

#	OBS-ID	Instrument (mode) MJD [d]	T_start MJD [d]	T_stop MJD [d]	T_mean[a] [h]	Duration[b] [h]	exposure[c] [sec]
1	00031403071	XRT [PC]	57203.453	57203.465	57203.459	0.28	979
2	00033861006	XRT [PC]	57205.452	57205.472	57205.463	0.48	1711
3	00031403072	XRT [PC]	57205.794	57205.805	57205.800	0.27	949
4	00031403074	XRT [PC]	57206.660	57206.670	57206.666	0.23	819
5	00033861007	XRT [PC]	57207.377	57207.394	57207.386	0.42	1478
6	00031403076	XRT [PC]	57207.521	57207.535	57207.528	0.33	1164
7	00033861008	XRT [PC]	57208.373	57208.390	57208.382	0.42	1471
8	00031403079	XRT [PC]	57208.916	57208.933	57208.925	0.41	1451
9	00031403078	XRT [PC]	57208.986	57208.996	57208.992	0.25	874
10	00031403080	XRT [PC]	57209.516	57209.526	57209.522	0.26	901
11	00081751001	XRT [PC]	57209.660	57209.783	57209.714	2.97	1763
12	00031403081	XRT [PC]	57210.379	57210.390	57210.385	0.26	909
13	00031403083	XRT [PC]	57210.309	57210.319	57210.314	0.24	852
14	00031403084	XRT [PC]	57211.509	57211.519	57211.514	0.24	854
15	00031403085	XRT [PC]	57211.717	57211.859	57211.786	3.41	1746
16	00031403086	XRT [PC]	57212.589	57212.992	57212.808	9.67	1988
17	00031403087	XRT [PC]	57213.050	57213.058	57213.055	0.20	717
18	00033861010	XRT [PC]	57218.177	57218.848	57218.498	16.1	5304
19	00031403107	XRT [PC]	57223.092	57223.962	57223.431	20.9	9168
20	00031403108	XRT [PC]	57226.474	57226.823	57226.639	8.37	6785
21	00031403111	XRT [PC]	57231.002	57231.478	57231.292	11.4	11170
22	00031403113	XRT [PC]	57235.248	57235.794	57235.495	13.1	10186
23	00031403115	XRT [PC]	57239.171	57239.521	57239.343	8.37	9742

[a] The average arrival time of all the photons during the multiple *Swift*/XRT snapshots.
[b] Defined as the time interval between the start of the first *Swift*/XRT snapshot and the end time last snapshot.
[c] Total *Swift*/XRT exposure time of all snapshots taken within the duration of the obs-id.

APPENDIX A: X-RAY OBSERVATION LOGS

APPENDIX B: ANGULAR PROFILE OF THE DUST SCATTERED X-RAY EMISSION

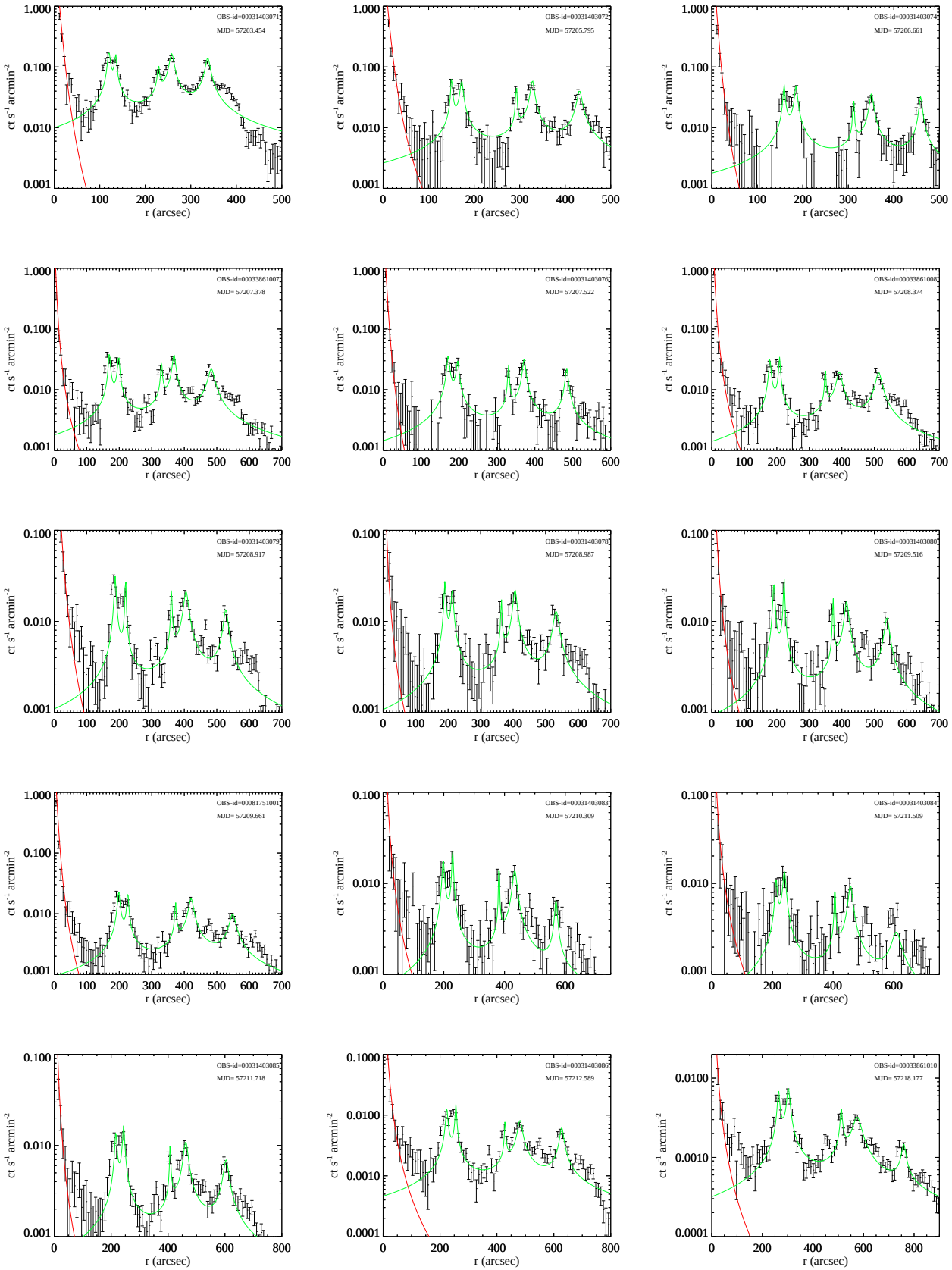

Figure B1. The background subtracted radial profile of the dust rings for a sample of the *Swift*/XRT observations covering the period MJD 57203.4 - 57218.2. The fitted model is composed by a King profile (red line) and five Lorentzian functions (green line).

Table B1. Peak position r_{0i} (in arcsec) of the five Lorentzian functions shown in Figs. 3 and B1 and the reduced χ^2 value of the global fit.

# #	OBS-ID	MJD[a] [d]	r_{01} [″]	r_{02} [″]	r_{03} [″]	r_{04} [″]	r_{05} [″]	χ^2/dof
1	00031403071	57203.459	120.1±0.8	134.9±0.8	229.0±0.8	258.1± 0.8	337.3±0.7	783/201
2	00033861006	57205.463	145.6±0.8	167.4±1.0	282.9±0.4	319.9± 0.8	418.0±0.9	919/236
3	00031403072	57205.800	150.6±0.5	172.5±0.8	292.5±0.3	327.9± 0.7	431.4±0.8	279/189
4	00031403074	57206.660	158.9±0.8	185.1±0.8	311.4±0.3	350.7± 0.8	458.9±0.6	159/156
5	00033861007	57207.386	169.5±0.9	198.1±0.9	329.8±0.6	368.4± 0.8	483.2±1.4	360/194
6	00031403076	57207.528	171.5±1.0	196.4±1.1	330.5±0.6	371.7± 0.8	484.0±0.8	250/168
7	00033861008	57208.382	178.7±1.0	208.6±0.8	349.1±0.5	392.1± 1.6	513.5±1.3	631/279
8	00031403079	57208.925	187.4±0.8	219.4±0.4	360.4±0.4	405.5± 1.2	527.7±1.3	549/272
9	00031403078	57208.992	190.1±1.0	212.7±1.3	363.6±0.8	405.7± 1.1	532.0±1.6	317/253
10	00031403080	57209.522	190.9±0.8	222.4±0.7	372.8±0.5	414.6± 1.3	538.6±1.5	329/267
11	00081751001	57209.661	198.4±1.1	226.2±0.7	373.0±0.8	421.0± 1.1	548.7±1.6	580/291
12	00031403081	57210.385	200.0±0.6	229.6±1.0	384.2±0.3	435.1± 1.3	566.6±1.6	308/255
13	00031403083	57210.314	198.2±1.4	229.1±0.8	381.8±0.3	433.6± 1.5	569.6±1.6	326/255
14	00031403084	57211.514	212.1±1.5	239.1±1.6	405.4±0.6	457.0± 1.6	608.±5.	250/245
15	00031403085	57211.786	216.5±1.1	243.9±1.0	407.4±0.7	462.3± 1.2	604.0±1.5	435/297
16	00031403086	57212.808	223.7±1.1	255.8±0.8	428.7±0.7	481.1± 1.4	627.7±1.3	545/325
17	00031403087[b]	57213.055	233.0±1.4	261.7±1.0	429.2±0.6	488.± 2.	637.4±1.2	234/237
18	00033861010	57218.498	264.0±0.9	302.8±1.0	512.2±1.0	575.± 2.	759.±2.	526/368
19	00031403107[c]	57223.431	299.3±1.2	343.8±1.2	572.62±0.9	644.7± 1.6	852.0±4.	635/376
20	00031403108	57226.475	319.2±1.2	362.9±1.5	614. ±2.	686.± 4.	880.±20.	447/361
21	00031403111	57231.292	350.0±2.	394.8±1.4	654.±9.	738.± 6.	> FOV [d]	432/369
22	00031403113	57235.495	370.7±1.5	418.3±1.6	not resolved [e]	not resolved [e]	> FOV [d]	406/361
23	00031403115	57239.343	388.4±2.	448.7±1.5	not resolved [e]	not resolved [e]	> FOV [d]	473/359

[a] The average time of the respective exposure (see also Table B1).
[b] Being an observation with small exposure time and low signal to noise, it will not be included in the analysis of the intensity profiles.
[c] The fifth ring was modeled by a Gaussian function for the fit.
[d] The fifth X-ray ring is outside the FOV and cannot be constrained.
[e] The peak count rate of the ring is too small to allow for a reliable determination of its peak position.